Tectonophysics 750 (2019) 262–279

Contents lists available at ScienceDirect

Tectonophysics

journal homepage: www.elsevier.com/locate/tecto

Integrated crustal model beneath the Po Plain (Northern Italy) from surface wave tomography and Bouguer gravity data

Rosaria Tondi[a,*], Alessandro Vuan[b], Alessandra Borghi[a], Andrea Argnani[c]

[a] Istituto Nazionale di Geofisica e Vulcanologia, Sezione di Bologna, Via Donato Creti, 12, 40128 Bologna, Italy
[b] Istituto Nazionale di Oceanografia e di Geofisica Sperimentale (OGS), Ctr. Ric. Sismol., Borgo Grotta Gigante 42c, 34010 Trieste, Italy
[c] ISMAR-CNR, Istituto di Scienze del Mare, Via Gobetti 10, 40129 Bologna, Italy

ARTICLE INFO

Keywords:
Po plain
3D crustal model
Surface waves
Bouguer gravity anomalies

ABSTRACT

To obtain a 3-D crustal density and shear-wave velocity structure beneath the Po plain, we exploit seismic records gathered from 2006 to 2014 and Bouguer gravity data assembled for the last estimation of the Italian Geoid. 2-D maps for both Love and Rayleigh fundamental mode at periods between 4 and 20 s are obtained applying a tomographic inversion. The defined local dispersion curves are then jointly inverted using a linearized scheme to obtain a 3-D isotropic shear-wave velocity model across the Po plain region. The model, transformed into density through a priori velocity-density relationships, is then the input of the Sequential Integrated Inversion algorithm, which enables us to recover a new 3-D density-shear wave velocity coupling and inferences on the lithology and tectonics.

Low and fast S-wave velocities are highlighted for the shallow Pliocene–Quaternary sediments along the foredeep, in front of the Northern Apennines, and for the presence of limestone units in the upper crust, respectively. Whereas sediment trends seem to be consistent with the results obtained, the Mesozoic carbonates, which are inherently characterized by high variability, are less resolved. A major result is the recovery of a high speed (3.3 km/s) - density (2.2 kg/m^3) structure in the upper crust (6–10 km) localized beneath the arcuate Po plain thrust front expanding from the external margin of the Ferrara arc toward the Alps and the Adriatic Sea. At the boundaries of this brittle body, we locate earthquakes of the Emilia 2012 seismic sequence and the historical seismicity. Mapping lateral discontinuities in density and shear wave velocity could provide insights in defining strengthening and weakening zones, and in focusing on transition zones often prone to earthquakes.

1. Introduction

The Po plain is the foreland basin of both the Alps and the Apennines (Fig. 1; Pieri and Groppi, 1981; Castellarin et al., 1985). The subsidence of this area is heavily influenced by the tectonic and geodynamic processes responsible for the formation and structuring the Alps and the Northern Apennines mountain systems (Fantoni and Franciosi, 2010; Ghielmi et al., 2013).

Foreland basins are characterized by thick successions of clastic sediments (gravels, sands, and silts) accumulated in relatively short geological time (Figs. 1 and S1). The space available for the deposition of these sediments is continuously created by the flexural subsidence due to the load of the rising chain. These deposits come from the mountain belt that is undergoing erosion, and their stratigraphic architecture reflects, more or less directly, the different tectonic phases that contributed to raising the Alps.

The Alpine chain, which is almost symmetrical with respect to its longitudinal axis, has produced two flexural basins: a proper foreland basin to the north (Molasse basin) and a retro-basin to the south (Po plain and Veneto-Friuli plain), the latter is partly connected to the south with the foreland basin originated by the load of the Northern Apennines (Fig. 1). These foreland basins of the Po Plain, even with different geological evolution, share a rapid deposition of Cenozoic heterogeneous clastic successions on a pre-orogenic substrate, mostly characterized by Mesozoic carbonate rocks. It is, therefore, common to find in the subsurface, even at relatively shallow depths, porous and permeable geological bodies able to accommodate and release various kinds of fluids (water, oil, gas) alternating with substantially impermeable formations, capable of physically isolating the previous ones. The outer fronts of the Apennine and Southalpine belts are buried under the Po Plain, and in some instances, the deformation is still ongoing, with tectonic structures capable of producing earthquakes (e.g.

* Corresponding author.
E-mail address: rosaria.tondi@ingv.it (R. Tondi).

https://doi.org/10.1016/j.tecto.2018.10.018
Received 12 December 2017; Received in revised form 8 October 2018; Accepted 14 October 2018
Available online 15 November 2018
0040-1951/

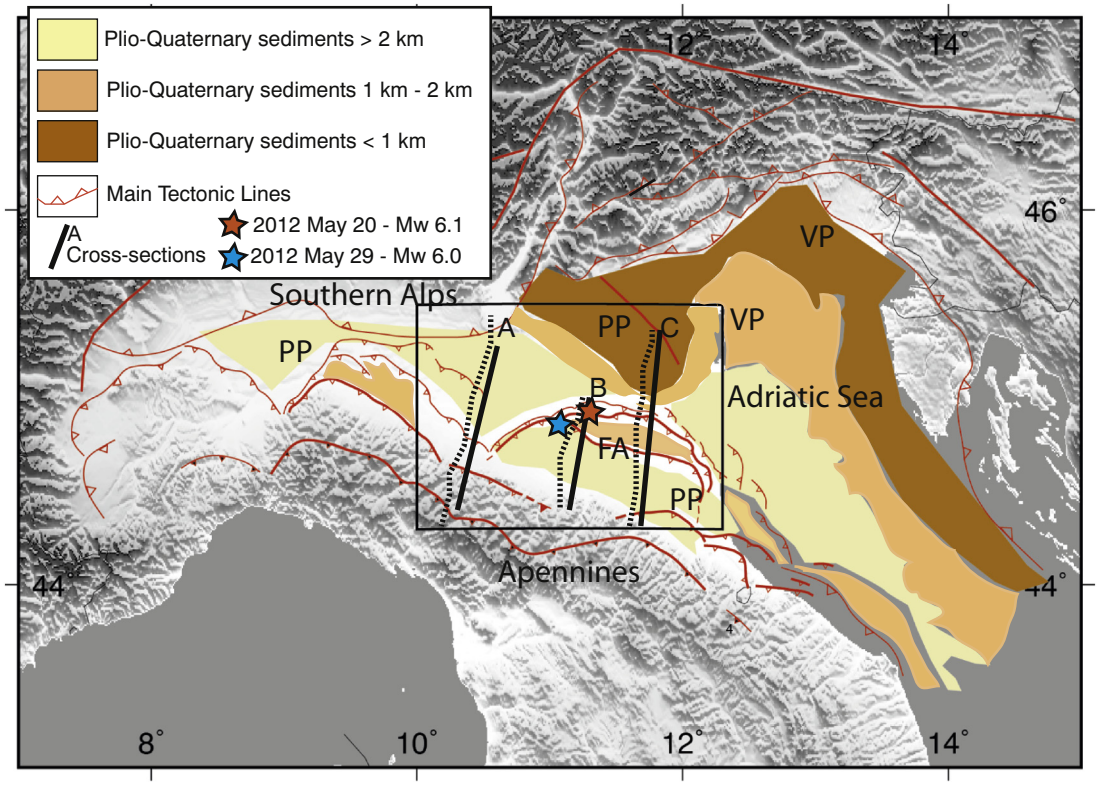

Fig. 1. Simplified map of the geological structures in Po Plain regions and surroundings (after Argnani et al., 2003 and Carannante et al., 2015). The traces of cross-sections A, B and C are also indicated. The box represents the study area of the surface wave tomography and the Bouguer gravity modelling. Stars indicate the two $M_W \geq 6$ mainshocks of the 2012 Emilia sequence. FA Ferrara Arc, PP Po Plain, VP Venetian Plain. Red thin lines represent the main tectonic lines (Serpelloni et al., 2016). (For interpretation of the references to colour in this figure legend, the reader is referred to the web version of this article.)

the Emilia 2012 earthquakes, Carannante et al., 2015).

Although being only characterized by a relatively moderate seismic hazard level, when compared to other areas in Italy, several earthquakes have occurred in the past both within the Po plain and in the adjacent foothills (ISIDE WORKING GROUP, 2010; Rovida et al., 2011), with the remarkable 2012 earthquake sequence (Meletti et al., 2012) that included two $M \sim 6$ shocks (see Fig. 1) due to thrust faulting (Pondrelli et al., 2012; Scognamiglio et al., 2012), located on the western Ferrara arc (e.g., Carannante et al., 2015 and references therein).

Because of the thick and extensive sedimentary cover, the complex geometry of the buried tectonic structures, and the lack of borehole seismic stations the seismological investigation of the Po plain area is challenging. Previous studies discussed the Po Plain as part of the broader Italian seismo-tectonic region in terms of seismicity (Chiarabba et al., 2005), seismogenic source characteristics and processes (Basili et al., 2008), present-day stress field and focal mechanisms (Montone et al., 2012; Pondrelli et al., 2006), and GPS analysis (Serpelloni et al., 2013). Other studies have concentrated on selected areas or specific seismo-tectonic related topics across the Po plain and the surrounding regions: Burrato et al. (2003) and Benedetti et al. (2003), adopted a geomorphological approach to identify the location of active thrust faults; Carannante et al. (2015) and Bonini et al. (2014) imaged the active faults in the Emilia area using reflection data; Montone and Mariucci (2015) studied the present-day stress field reanalyzing the stratigraphic profiles of wells and available sonic logs located in the plain and the surrounding regions.

As regards to three-dimensional modelling, which is a valuable tool to tackle highly complex geological structures. Turrini et al. (2015), integrated the information from geological (Digital Earth Model, wells, isobath-maps, cross-sections, outcrop-trends) and seismological datasets to recover a comprehensive 3D seismo-tectonic geological volume of the crustal Po plain region. Similarly, Molinari et al. (2015), built a 3D model of the Po plain sedimentary basin, from the assemblage of extensive geological information available in the literature, and used it to compute the seismic response for the 2012 earthquakes. Vuan et al. (2011) verified the effectiveness of surface waves studies to long period strong motion within large and deep sedimentary basins like the Po and Venetian plains, which they reconstructed on the base of geophysical information from oil exploration and research. All these models represent a powerful tool to unravel the basin seismo-tectonic complexity. However, the inherent uncertainty in the assembled geological and geophysical information, the patchy hypocentre occurrence with highly concentrated clusters and the need to enhance the coverage of seismic stations within the Po plain limit the improvement of crustal images and the detailed definition of regional-scale features.

To compensate for this lack of knowledge, we jointly exploited the information given 1) by the surface wave data gathered from 2006 to 2014 seismicity and 2) by 73,590 gravity observations extracted from the Italian gravity database Italgeo05 (Barzaghi et al., 2007; Borghi et al., 2007). Seismic velocity models from surface-wave and compressional-wave tomography are frequently used as a reference to calibrate the interpretation of gravity data, being the inversion of density anomalies a highly non-unique process. On the other side, surface wave higher modes are often difficult to separate from the fundamental one, and multipathing effects complicate the modal pattern especially in deep sedimentary basins such as the Po plain. In this context, regional gravity information comes to the aid, having the highest resolving power at shallow depths.

The Sequential Integrated Inversion (SII) procedure (Tondi et al., 2012) is used to recover the 3D pattern of elements, with lateral sides of 0.033° and variable depth, for crustal (a) isotropic shear-wave speeds, (b) density-shear-wave velocity (ρ-v_S) correlation coefficient and (c) densities which explain both surface-waves and gravity data

information.

2. Data

2.1. Seismic data

The 2012 Emilia seismic sequence and other earthquakes occurred in northern Italy from 2006 to 2014 allowed gathering a significant dataset to investigate the Po plain crustal properties. We exploit accelerometric and velocimetric seismic records from national and regional networks to measure Rayleigh and Love group velocity wave dispersion properties at short periods (4 s – 20 s). Group velocity from recorded earthquakes are preferred to ambient noise phase velocity measurements because of: 1) the poor density of seismic stations that are recording data in continuous mode within the Po plain (see Fig. 1 in Molinari et al., 2015), 2) the low data quality of the few seismic stations within the deep basin (seismic stations are generally deployed at surface on soft sediments), 3) most of the seismic stations within the Po plain are accelerometers recording earthquakes in triggered mode.

We select shallow depth (hypocentre < 30 km) earthquakes with magnitude > 3.6 recorded in the distance range from 50 km to 400 km. In the period range 4 s – 20 s, lower magnitude earthquakes show no efficient propagation of surface waves at distance and source-receiver paths shorter than 50 km are not considered because fundamental mode surface wave trains are not separated from higher modes and shear-waves.

Travel times are determined using epicentral locations and origin times taken from national agencies. Group velocity dispersion curves are measured using an iterative application of a set of Gaussian multiple filters. The selection of the dispersion curves represents a critical point, and it must be guided by regional crustal models (Vuan et al., 2011; Sugan and Vuan, 2014; Barnaba et al., 2014). A semi-automatic phase match filtering is used to isolate the fundamental mode from interfering higher modes, and body waves.

The number of the Rayleigh and Love dispersion measurements, performed in the period band from 4 to 20 s, is approximately 5000 and 2500, respectively. The Po plain area is characterized by significant lateral variations in structure, which can result in multipathing and refraction or reflection of wave paths when they cross major structural boundaries such as the Alps and the Apennines. The cluster analysis on common paths and the subsequent quality check, to avoid outliers, reduced the average number of reliable dispersion curves to approximately 3000 and 1500 for Rayleigh and Love waves, respectively. In Figs. 2 and S2 we show the 6 s Rayleigh and Love wave path coverage in the Po plain and, the number of paths as a function of the measured period after removing outliers and clustering. Rejected measurements at shorter periods (2 s) are mostly due to interfering higher modes that hamper an accurate estimation of the group velocities (see the histogram in Fig. S2).

Surface wave depth sensitivity is dependent on the period: the longer the period, the deeper the waves sample within the earth. The sensitivity curves are the Fréchet derivatives of the group velocities of the fundamental mode Love and Rayleigh waves with respect to shear-wave velocities at different depths. The derivatives are computed for the Po plain reference earth model (see Vuan et al., 2011) at different periods, and are shown in Fig. 3. From contouring, it is possible to infer the depth sensitivity of the group velocity dispersion curves in the 4 – 20 s period range. We observe a low sensitivity at approximately 3–7 km of depth for the Rayleigh waves. At the same depth interval, Love waves behave differently demonstrating the need to use both Rayleigh and Love wave data to resolve the crustal model at shallow depth.

2.2. Bouguer gravity anomalies

The terrestrial gravity data set used in the computation of the crustal density in the Po Valley has been extracted by the validated gravity database formed for the last estimation of the Italian geoid, called Italgeo05 (Barzaghi et al., 2007; Borghi et al., 2007). In the area bounded between 44°N and 46°N in latitude and between 7.5°E and 12.5°E in longitude, 73,590 values of the free-air anomalies are available (Fig. 4 a), with a spatial resolution strictly related to the topography of the area (few data in the sea basins and in high mountains regions).

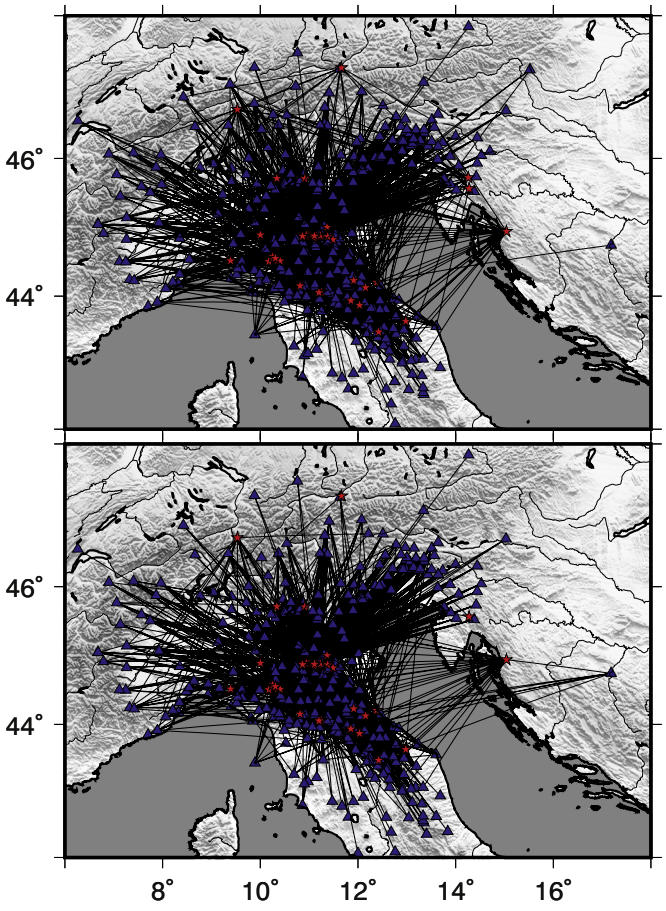

Fig. 2. Path coverage map at 6 s (top) Rayleigh and (bottom) Love waves. Blue triangles and red stars mark the seismic stations and seismic events, respectively. (For interpretation of the references to colour in this figure legend, the reader is referred to the web version of this article.)

To match seismological information to gravity ones, the required data resolution was approximately 1 km. Hence, to improve the computation speed, the original dataset has been gridded on a 1 km × 1 km interval (Fig. 4 b), using a weighted moving average approach with the data weighed with the inverse of the cube of the distance from the grid knot.

The gravimetric inverse problem is an ill-posed problem so, to impose the existence and the uniqueness of the solution, it is necessary to perform some regulations of the gravity data, as the computation of refined Bouguer gravity anomaly. The Bouguer gravity anomaly reduction describes the earth as composed of two layers with a fixed density contrast and without topography, so it represents a suitable type of observation to investigate crustal density anomalies. According to Heiskanen and Moritz (1990), the Bouguer gravity anomaly can be computed for a gravity station P as:

$$\Delta g_B = \Delta g_{FA} - A_B + A_{TC} \quad (1)$$

where:

Δg_B = Bouguer anomalies

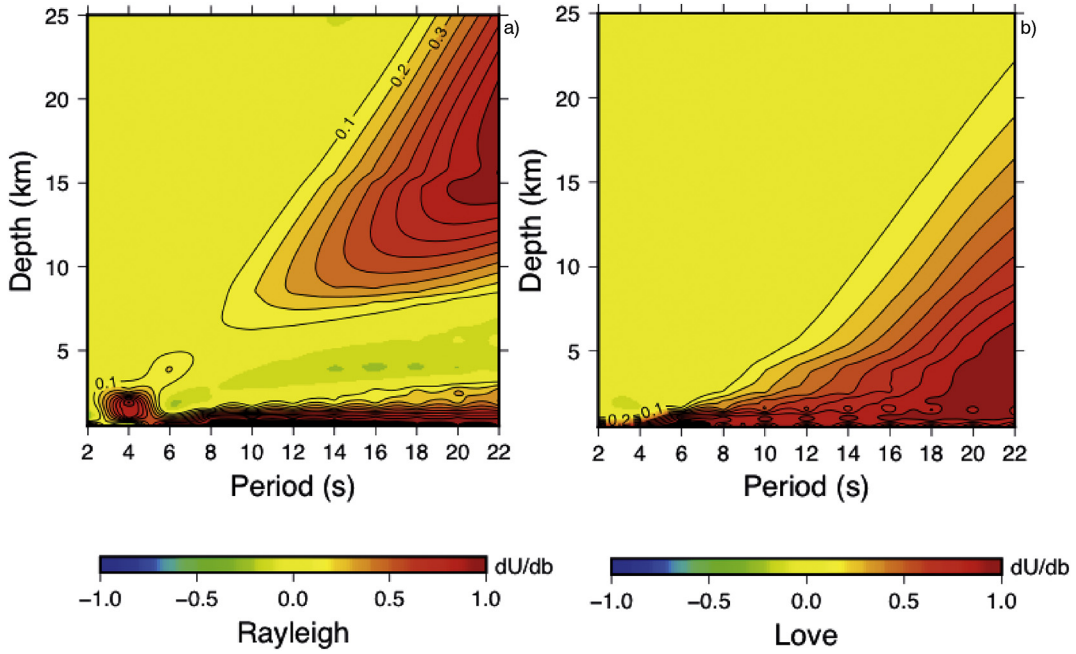

Fig. 3. Depth sensitivity of surface waves. The sensitivity curves are the Fréchet derivatives of the group velocities (dU) of the fundamental mode (left panel) Rayleigh and (right panel) Love waves with respect to shear-wave velocities (db) at different depths. The derivatives were computed for a Po plain reference model (Vuan et al., 2011).

Δg_{FA} = Free-air anomalies, that is the values of the absolute gravity reduced for the reference normal gravity γ and corrected for the height of the point P with respect to geoid surface, that is $\Delta g_{FA} = g - \gamma + F$, where F is called free-air reduction

$A_B = 2\pi G\rho H$ = gravity of the Bouguer plate, where H is the orthometric height of the point in meters; G is the gravitational constant; ρ is the crustal density

A_{TC} = Terrain correction with density ρ

The Terrain Correction term (A_{TC}) is introduced in the formula to have the so-called refined Bouguer gravity anomaly (Fig. 4 b), where the systematic effects due to the topography, that is the gravity effects of the masses above the geoid, are removed. This contribution is computed by integration of gravity effects of the terrain up to a distance of 120 km, modelled by rectangular prims of constant density, using the TC program of the GRAVSOFT software package (Forsberg and Tscherning, 2008). The dimensions of the prisms (3″ × 3″) are determined by the Italian DTM (Digital Terrain Model) based on SRTM3 and NOAA bathymetry, integrated along the coast with the 5″ × 7.5″ Italian bathymetry (Borghi et al., 2007). The density value of the prisms is chosen to exploit two different optimization methods (see Caratori Tontini et al., 2007), which have given the same optimal result of 2.45 g cm^{-3}.

The resulting Bouguer gravity anomaly map (Fig. 4b) is characterized by a main gravity low spanning [−180,–120] mgals in the lower left side of the studied area, below the provinces of Parma, Reggio Emilia and Modena, and positive anomalies in the range of [0,60] mgals below the Venetian provinces.

3. Methods

Our integrated approach (SII, Tondi et al., 2012) involves in finding the maximum of a likelihood function (L) that relates the density earth structure (ρ) to our Bouguer gravity observations (**g**) and to the seismic velocity structure (***v***) through three types of information: (i) gravity data, (ii) update of the shear velocity model computed by nonlinear inversion of the seismological data-set (Δ***v***), and (iii) the physical correlation between the density and the velocity parameters (**α**, C_{mm}):

$$L(\Delta g, \Delta\rho, \Delta v) = \exp\left\{-\frac{1}{2}[\Delta g - G\Delta\rho]^T C_{gg}^{-1}[\Delta g - G\Delta\rho]\right\} \exp\left\{ -\frac{1}{2}[\Delta\rho - \alpha\Delta v]^T C_{mm}^{-1}[\Delta\rho - \alpha\Delta v]\right\} \quad (2)$$

The resulting SII algorithm allows the iterative estimation of the update (Δρ) to the starting model (ρ_0):

$$\Delta\boldsymbol{\rho} = (\boldsymbol{G}^T C_{gg}^{-1}\boldsymbol{G} + C_{mm}^{-1})^{-1}(G^T C_{gg}^{-1}\Delta\boldsymbol{g} + \alpha C_{mm}^{-1}\Delta\boldsymbol{v}) \quad (3)$$

where **G** is the matrix of the partial derivatives of the Bouguer gravity observations (**g** = [g_1, g_2, …g_N], n ∈ [1,N]) relative to the density model parameters (ρ = [ρ_1, ρ_2, … ρ_M], m∈ [1,M]), $\mathbf{C}_{gg}$ is the square diagonal covariance matrix of the gravity data uncertainties, $\mathbf{C}_{mm}$ is the covariance matrix that takes into account the error propagation from the velocity to the density model, $\Delta\mathbf{g} = (\mathbf{g}^{OBS} - \mathbf{g}^{(i)})$ the residual gravity vector with respect to the i-th model predicted gravity response, **α** = [α_1, α_2, …α_M], m∈ [1,M] the velocity-density gradient vector, in the same parametrization as the model, Δ***v*** (***v*** − $\boldsymbol{v}_0$) the seismological update to the starting velocity model $\boldsymbol{v}^0$ of dimension M.

Following the flowchart in Fig. 5 the starting point of the proposed method is the estimate of the best-fit shear-wave velocity update (Δ***v***) to the starting velocity model (step 2). We dedicate the following section to its description.

3.1. Surface waves tomography

3.1.1. Regionalization of the dispersion measurements

The Po plain tomography is performed using two different methods: the Yanovskaya et al. (2000) tomographic codes and the Fast Marching Surface Tomography (FMST) package by Rawlinson and Sambridge (2003). Yanokskaja'çode is a 2D Bakus-Gilbert approach (Ditmar and Yanovskaya, 1987; Yanovskaya and Ditmar, 1990) based on first-spatial gradient smoothness constraints for local or regional application. The method, extensively used in group velocity tomography (e.g. Ritzwoller et al., 1998; Vuan et al., 2000; Vuan et al., 2014), uses iterative ray tracing of surface waves and the quality of the solution is estimated by comparing the initial mean square travel-time residual with the remaining unaccounted residual. FMST by Rawlinson and Sambridge

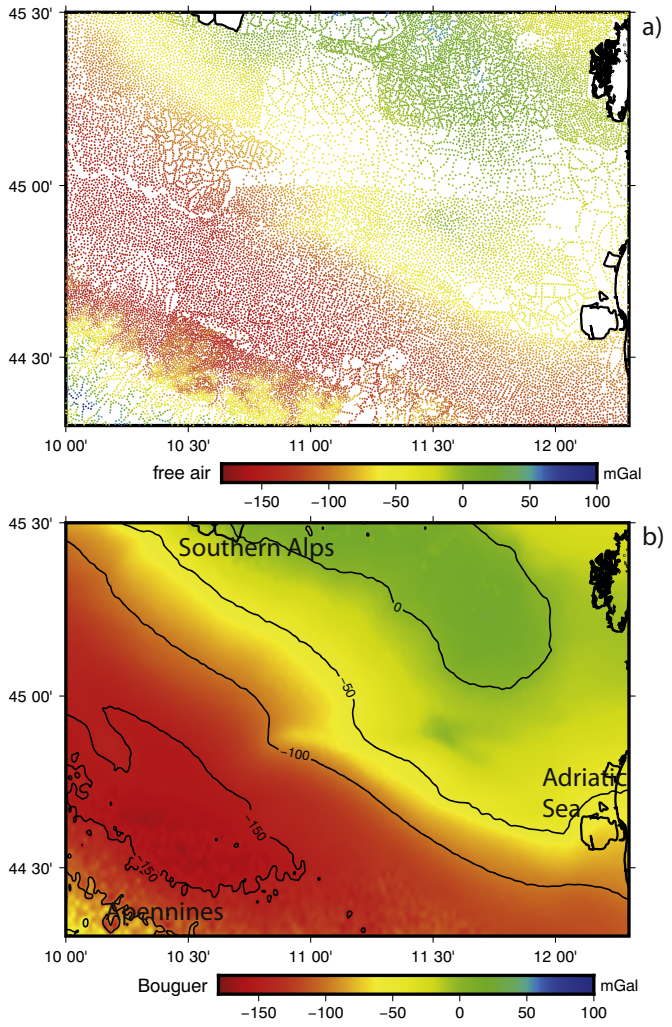

Fig. 4. (top) Free-air gravity anomalies in the studied area extracted by the Italian database (Barzaghi et al., 2007; Borghi et al., 2007). (bottom) Values of the Bouguer anomalies computed on a 1 km × 1 km grid.

(2003) solves the forward problem using a grid-based eikonal solver known as the fast marching method (e.g. FMM Sethian and Popovici, 1999), and the inverse problem using a subspace inversion method. The method is iterative and non-linear. The inversion step assumes local linearity, but repeated application of FMM and subspace inversion allows the non-linear relationship between velocity and travel time perturbations to be reconciled. Yanokskaja'çode and FMST do not require any a priori parameterization or truncation of any expansion, and both are widely tested. The Yanovskaya et al. (2000) method can reject data when the travel-time residual is three times higher than the remaining unaccounted residual, in which case the solution is recalculated. The density of paths, azimuthal coverage, and average path length, control the resolution of the dataset. Both the Yanovskaya et al. (2000) tomographic code and the Fast Marching Surface Tomography (FMST) package by Rawlinson and Sambridge (2003) obtain consistent results in the regionalization of the measured dispersion curves.

Rayleigh wave velocities depend principally on the vertically polarised shear-wave and compressional-wave velocities and densities in the crust and upper mantle. The velocity of Love waves depends primarily on the horizontally polarised shear-wave velocity and the density. The Po plain area is here parameterized by a 2-D mesh consisting of square elements with sides of 0.2°. Tomography is repeatedly performed using different origin coordinates of the grid to obtain four slightly different images from every 0.1° staggered grid. Staggering variable grids, and averaging the corresponding values instead of inverting a single more refined model presents the advantage of reducing possible inversion instabilities and ambiguities. In so doing, we get a more complex image with higher nominal resolution.

We calculate the group slowness at the nodes of each square from dispersion measurements on intersecting propagation paths, and a four-point linear interpolation is used to evaluate the model within each square element in the area. The choice of a 0.2° grid is made in agreement with the tomography resolution that is estimated both by performing checkerboard tests and by calculating the averaging length and azimuthal dependence. Path density, azimuth, and average path length influence the dataset resolution. Because small variations in the observed data can cause significant differences in the resulting inverted model, it is necessary to restore stability by using regularization. We select a regularization parameter, so that (1) the regionalized velocities are within the velocity range defined by the individual observed dispersion relations and (2) the final unaccounted travel-time residuals are distributed randomly (Yanovskaya et al., 1998). Calculations of group velocity maps are made for several regularization parameters, $\alpha = 0.05, 0.1, 0.2$ and 0.3. The lower the parameter α, the more we get a sharper solution region with a high solution error, whereas an increase in α leads to a smoother solution region with a lower solution error. Finally, we use the value of $\alpha = 0.2$, which gives relatively smooth maps with small solution errors.

In tomography, the knowledge of the resolution is important to estimate the minimum resolvable feature for a given sample and to determine those features that could represent a numerical artifact. Yanovskaya (1997) and Yanovskaya et al. (1998) proposed the use of two parameters as resolution estimators. The mean size of the averaging area is the first parameter (L) that can be defined as:

$$L = [\mathrm{smin}(x, y) + \mathrm{smax}(x, y)]/2 \quad (4)$$

where smin(x, y) and smax(x, y) are the smallest and the largest axes of an ellipse that the averaging area can be approximated to, centred at each examined point (x, y). As the resolution is closely correlated to the density of the crossing ray paths in each cell, it is clear that small values of the mean size of the averaging area (corresponding to high resolution) should appear in the areas that are crossed by a large number of ray paths and vice versa.

The stretching of the averaging area is the second parameter, which provides information on the azimuthal distribution of the ray paths and is given by the ratio:

$$2[\mathrm{smax}(x, y) - \mathrm{smin}(x, y)]/[\mathrm{smax}(x, y) + \mathrm{smin}(x, y)] \quad (5)$$

Small values of the stretching parameter imply that the paths are more or less, uniformly distributed along all directions. Hence the resolution at each point can be represented by the mean size of the averaging area. On the contrary, large values of this parameter (usually > 1) mean that the paths have a preferred orientation and that the resolution along this direction is likely to be quite small (Yanovskaya, 1997). Averaging area and stretching correspond to “correlation length” and azimuthal dependence, respectively.

The resolution is initially determined using the correlation length of the effective smoothing area as estimated by Yanovskaya et al. (1998), and it is less than or equal to 20 km in the area. Furtherly, a more common approach to estimating the tomographic resolution, based on synthetic checkerboard tests, is applied by using different grids and FMST codes by Rawlinson and Sambridge (2003). The results, shown in checkerboards of Fig. 6, confirm the correlation length calculated with the Yanovskaya et al. (1998) technique. Checkerboard results are shown for Rayleigh and Love waves at periods of 4, 8, 12, 16 s. 20 km lateral discontinuities of the synthetic model are resolved by source-receiver paths shown in Fig. 2. Results of the checkerboard tests show that ray paths sample the selected area uniformly in the period range 4–20 s. Moreover, a similar resolution is obtained for Rayleigh and Love waves.

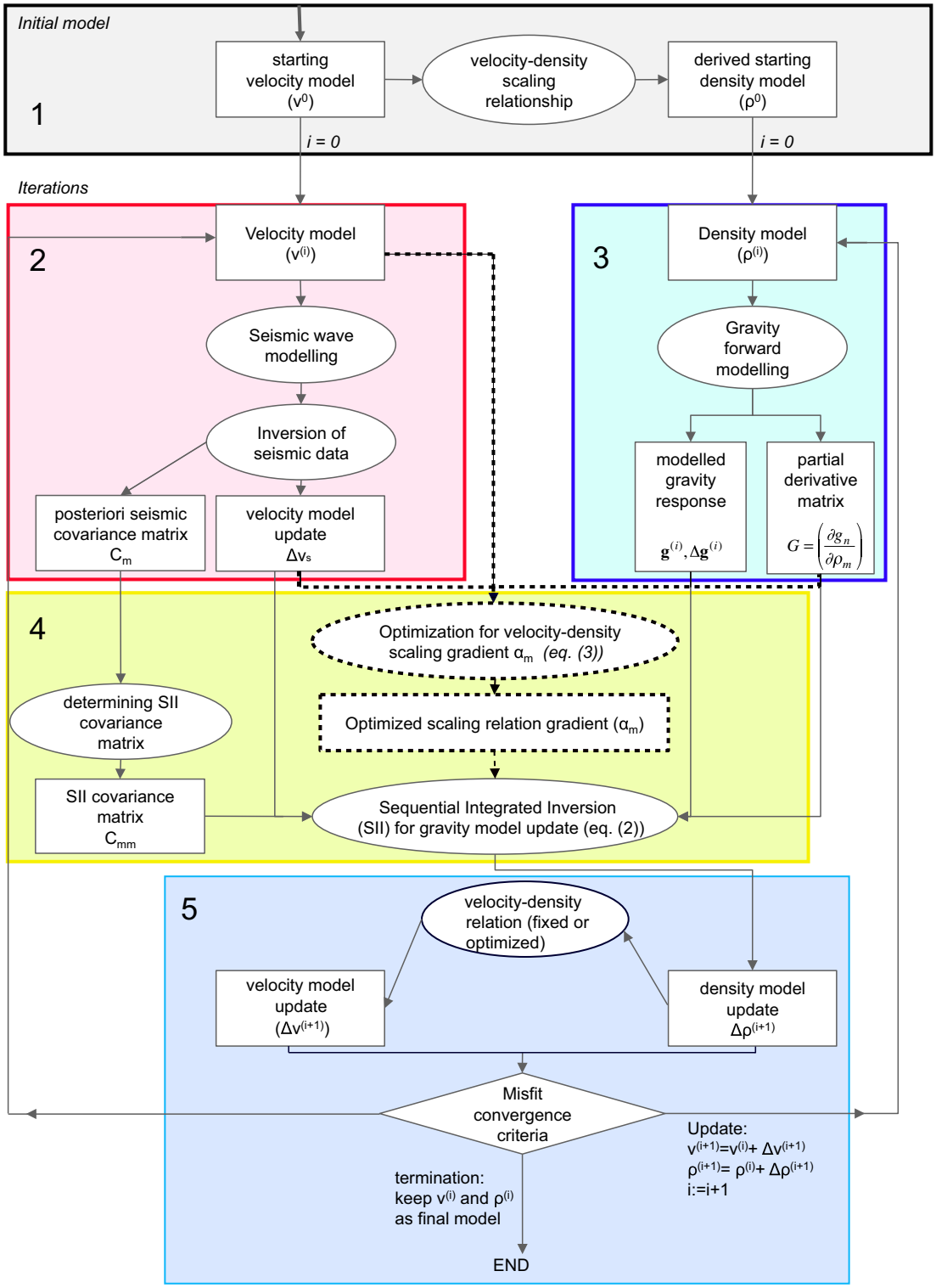

Fig. 5. Flowchart of the inversion procedure, including optimization of density and velocity (indicated by black dashed lines). Different colors indicate the relevant steps of the procedure.

3.1.2. S-wave velocities

Shear-wave velocity profiling from surface wave dispersion curves is a non-linear inversion problem. To date, numerous papers have examined the surface wave inversion problem using global or heuristic algorithms (e.g., Beaty et al., 2002; Wathelet et al., 2004; Yamanaka, 2005). Global method solutions typically require large computational efforts because they are based on genetic or Monte Carlo algorithms. An alternative approach is a linearized inversion, which has been extensively applied using least squares methods (e.g.,Wiggins, 1972; Nolet, 1981; Gabriels et al., 1987; Xia et al., 1999; Herrmann, 2013).

The local dispersion relations retrieved from the tomographic maps for both the Love and Rayleigh fundamental mode are jointly inverted using a linearized scheme (Herrmann, 2013) to obtain refined isotropic shear-wave velocity models across the Po plain. The shear-wave velocity models described in Vuan et al. (2011) are considered a reference in the inversion when its predicted dispersion values are consistent with

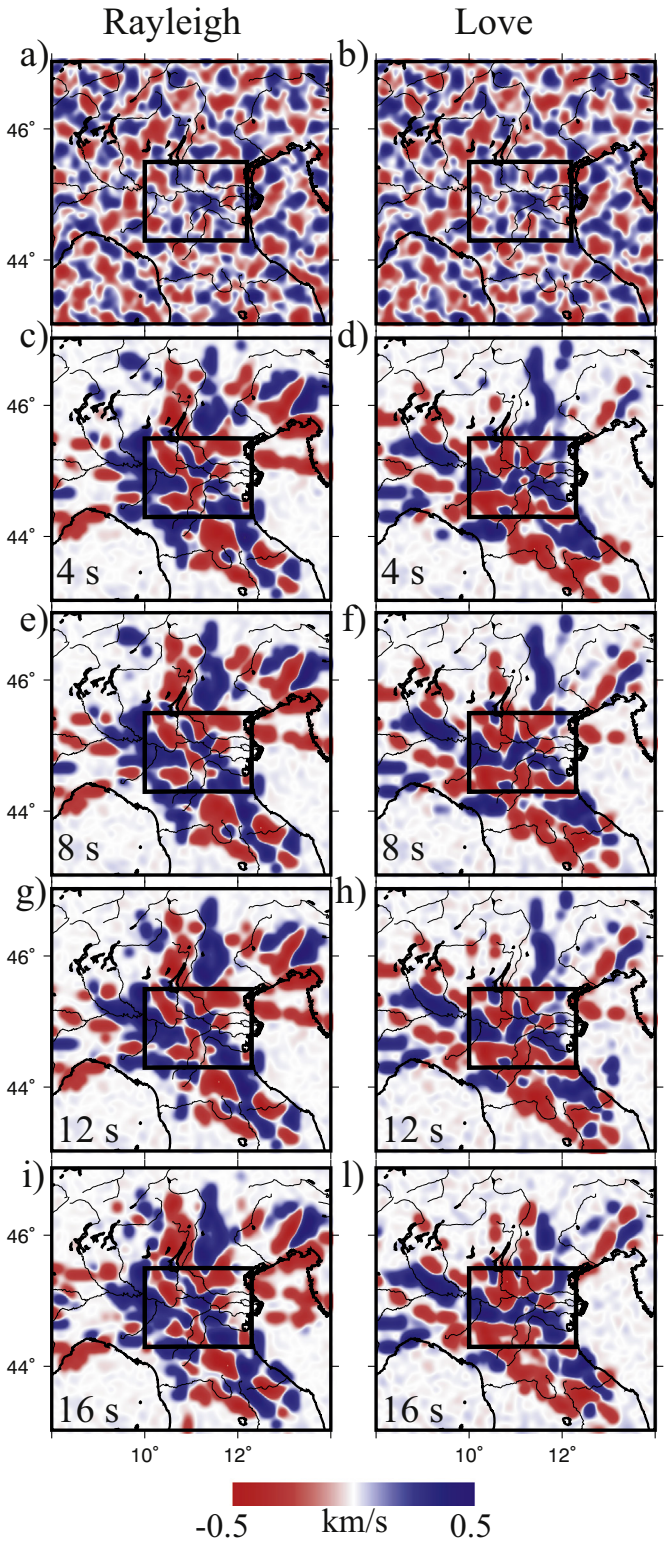

Fig. 6. Checkerboard synthetic test with 0.5 km/s distributed velocity anomalies for a) Rayleigh waves and b) Love waves input models. We add to the regular synthetic checkerboard a random structure with perturbations in excess of 50% relative to the background. The panels c, e, g, i) show reconstruction for Rayleigh group velocities at 4, 8, 12, 16 s respectively. Love wave velocity reconstruction at 4, 8, 12, 16 s is shown in d, f, h, l panels respectively.

local observations. When group velocities in specific sub-regions are inconsistent with local dispersion curves at periods longer than 10 s, we use the reference shear-wave velocity models from EPcrust (Molinari and Morelli, 2011) or, as an alternative and only in few cases, from Malagnini et al. (2012).

Table 1
The starting 1D shear-wave velocity structure below the studied area (v^0). Density is recovered from v^0 with the starting scaling relationships (see text for more information).

Depth interval (km)	Vp (km/s)	Vs (km/s)	Density (kg/m^3)	Layer
0.00–1.00	1.5	0.6	1.00	Sediments
1.00–2.00	1.8	0.9	1.75	"
2.00–3.00	2.16	1.2	1.90	"
3.00–3.50	3.50	2.10	2.10	Consolidated sediments
3.50–4.00	4.15	2.40	2.32	"
4.00–5.00	4.75	2.75	2.37	"
5.00–6.00	5.33	3.05	2.41	Upper crust
6.00–10.00	5.88	3.40	2.44	"
10.00–20.00	6.34	3.67	2.51	Middle crust
20.00–30.00	6.80	3.93	2.75	Lower crust

The Love and Rayleigh group velocity measurements sample with maximum sensitivity depths that vary between approximately 1 km and 20–25 km. At these depths, the crustal structure is modelled as a stacking of N homogeneous isotropic layers that are each defined by compressional and shear wave velocity, thickness, density, and attenuation. The shear-wave velocity is the only independent parameter that is optimized for the inversion. The compressional-wave velocities and densities, which are needed for the computation of the dispersion curves, are shear-wave-dependent parameters that are iteratively changed during the linearized inversion accordingly with Nafe and Drake (1957) experimental measurements for the sediments ($v_S \leq 2.58$ km/s) and Brocher (2008) for higher velocities. Other parameters of the model, such as thickness and attenuation are fixed a priori. Our strategy of inversion is guided by seeking iteratively for solutions that are linearly close to the shear-wave reference model (Table 1) (Parker, 1994). This procedure allows us to identify a reliable solution that fits the surface wave data and facilitates the computation of the associated errors (Gabriels et al., 1987). Uncertainties related to the optimized shear-wave velocities are determined by considering several different parameterizations for the inversion procedure, that is, the number of layers, the smoothness of the perturbation function and the compressional to shear-wave velocity ratio. In general, there is a trade-off between resolution (the number of layers in a specific depth range of the model) and variance. The robustness and stability of the inversion algorithm are guaranteed using a procedure, which checks the dispersion curve sensitivity about the applied perturbations to limit the number of inversions. Moreover, the application of smoothing constraints prevents large variations between layer velocities. Two criteria are used to accept a model: (1) the group velocity curves compared to any given period must lie within the uncertainty bounds of the observed data (0.040 km/s), and (2) the root mean square of the difference between the calculated curve and the observed data must be < 0.020 km/s. After the inversion, a simple linear interpolation scheme between the centres of the cells is adopted and 3D images of the shear-wave velocity structure of the Po plain are obtained.

3.2. The physical correlation between the density and the velocity parameters

The combination of information coming from seismic and gravity data into a single inversion scheme is based on the optimum choice of the physical relationships between the seismic velocities and bulk densities. To ensure this objective:

1. The 3-D velocity and density models share the same parametrization.

2. We assume a node-dependent linear relationship: $\rho_m = \alpha_m v_m + \beta_m$, m∈ [1,M], i.e. upon a-priori information, we can use different relationships (correlation coefficients α and β) for different rel ρ-v_S scaling relationships.
3. Through the maximization of Eq. (2) with respect to α, taking in account that in explicit linear form $\mathbf{g} = \mathbf{G}\boldsymbol{\alpha}(m)\boldsymbol{v}$, $\boldsymbol{\alpha}$ is now inverted and optimized independently for each model parameter:

$$\frac{[(G^T C_{gg}^{-1} G)^{-1}(G^T C_{gg}^{-1} g)]_m}{v_m^0 + \Delta v_m} \quad (6)$$

with $v_m{}^0$, m∈ [1,M], the starting velocity model;

4. The $\mathbf{C}_{mm}$ matrix takes into account the error propagation from the velocity to the density model

$$\sigma(\boldsymbol{\rho}_m) = \boldsymbol{v}_m \sigma(\alpha_m) + \alpha_m \sigma(\boldsymbol{v}_m) + \sigma(\beta_m) \quad (7)$$

where σ(v_m) is taken from the square roots of the diagonal elements of the a posteriori seismic covariance operator (0.250 km/s for depths from 0. to 4 km, 0.150 km/s from depths from 4 to 8 km and 0.80 km/s for depths from 8 to 20 km), σ(α_m) and σ(β_m) are the uncertainties in the coefficients of the scaling ρ_m-v_m relationship.

To control the amount of variation and to allow for correct changes in the parameter values, the values on the main diagonal of $\mathbf{C}_{mm}$ matrix (under the assumption that there is no correlation between the errors in each node) are chosen for an optimum trade-off between the data variance and the solution variance. Through the comparison of the gravity kernel ($\mathbf{G}^T\mathbf{C}_{gg}{}^{-1}\mathbf{G}$) and $\boldsymbol{C}_{mm}{}^{-1}$, we can conveniently assign σ(α_m) and σ(β_m) uncertainties and obtain over-regularized solutions where the density model remains close to the seismic model (high values of $\boldsymbol{C}_{mm}{}^{-1}$) or under-regularized solutions where the gravity information gives a significant contribution during the optimization process (low values of $\boldsymbol{C}_{mm}{}^{-1}$). This enables the complementarities of the seismological and gravity data sets to be exploited, and reliable solutions to be also obtained below the seismic depth resolution.

Starting relationships between the shear-wave crustal velocities and density values, as required by step 1 in Fig. 5, are derived from Nafe and Drake experimental measurements (Nafe and Drake, 1957) for the sediments ($v_S \leq 2.58$ km/s) and Brocher (2008) for higher velocities. To account for additional dependencies on a wide range of factors, such as the presence of fluids or compositional variations, we allow the density-velocity scaling to vary laterally during the inversion, through (6), thus creating a fully 3-D relationship between the density and the shear-wave velocity (Fig. 7).

3.3. Gravity data inversion

From the 10 layers 1D a priori velocity model ($\boldsymbol{v_0}$) (Table 1) we obtain the starting density model (ρ_0) with the above specified scaling relationships. Hence, with the transformed 3-D grid of density values in the earth volume of 2.4° × 1.2° × 30 km, we define 45,917 polyhedral bodies of 0.033° × 0.033° and variable height. To counteract edge effects, the model is boxed into a region of 8° × 4° × 50 km.

The expression that was derived by Pohànka (1988), for a polyhedral body with a density that is linearly dependent on some coordinates, is used for the computation of the three components of the gravity field (Tondi and de Franco, 2006) and the partial derivatives of each gravity measurement $\mathbf{g}_n$ with respect to each density model parameter ρ_m (step 3):

$$\mathbf{G} = \left[\left(\frac{\partial g_n}{\partial \rho_m}\right)_{n,m}\right]^{NxM} \quad (8)$$

The use of polyhedral bodies with linearly varying density enables us to appropriately match the density with the shear velocity parametrization during the sequential integrated modelling. As we work with Bouguer anomalies, tests are undertaken at each step to choose the appropriate background density, which is the density that minimizes the difference between the calculated vertical component of the gravity field and the observations (Δ**g**). The computations are carried out in Cartesian coordinates, and Vincenty formulas (Vincenty, 1975) are used to move from the geographic to the Cartesian coordinate systems, and vice-versa.

For all the gravity data the a-priori error (the square root of the diagonal elements of $\mathbf{C}_{gg}$) is set equal to 1.0 mGal, because no other information is available; the seismological update to the starting velocity model (Δ$\boldsymbol{v}$), obtained as described in Section 3.1, is interpolated through a tricubic B-splines function from the density grid, and we proceed to step 4 of the flow chart (Fig. 5) with the optimization of the density-v_S scaling relationships (6) and of the density values with (3).

As illustrated in Fig. 5, the last step (point 5) of the SII procedure is the update of the density and velocity parameters and the evaluation of the results.

The gravity data misfit is expressed as the rms of the gravity residuals for each n observation:

$$\text{rms} = \sqrt{\frac{\sum_{n=1}^{N}(g_n^{obs} - g_n^{(i)})}{N}} \quad (9)$$

The a posteriori standard deviation, associated with the updated density parameters ($\rho_m{}^i = \rho_m{}^{i-1} + \Delta\rho_m{}^i$), is calculated as:

$$\sigma\rho_m^i = \alpha_m^i\, \sigma(v_m^{i-1})\left[1 - \left(VarRed(g^i)\,\frac{d_{mm}}{\max(dmm)}\right)\right] (\text{m} = 1,...\text{M})\ (\text{i} = \text{the current iteration}) \quad (10)$$

which is the propagation of uncertainty from the velocity to the density model, weighted with the gravity variance reduction VarRed (g^i), and the information provided by the gravity data (d_{mm} the diagonal elements of the gravity kernel ($\boldsymbol{G}^T\boldsymbol{C}_{gg}{}^{-1}\boldsymbol{G}$)).

The optimization process should be repeated until the fit to the observations deteriorates with respect to the former iteration. Differently from the surface-wave inversion, which is a nonlinear optimization problem, gravity is a linear function of density and as a consequence the minimization of the gravity residual vector is immediate.

3.4. Summary of the method

A summary of the used method is reported step by step:

1) building of the starting velocity model and transformation of it into density through a priori 1-D density-v_S scaling relationships;
2) inverting of local Rayleigh and Love wave group velocity curves from fundamental mode observed group velocity and estimation of the updates to the velocity model (Δ$\boldsymbol{v}$);
3) solving of a 3D forward gravity problem;
4) updating of the density model with the constraint of Δ$\boldsymbol{v}$ and optional optimization of the velocity-density scaling gradient;
5) computing of the new velocity model from the best fit density model and the estimated velocity-density scaling relationships and evaluation of data misfits and of the quality of the solution.

In this study we keep this one-iteration model as our final model because we believe that a better fit can be achieved only with a more precise seismic information (lower data uncertainties and more uniform coverage).

4. Results

We obtain Rayleigh and Love group velocity tomography maps in the period range from 4 to 20 s. The 4 s to 10 s Rayleigh waves sample the upper crust and basin sediments at depths ranging from 1 km to 8 km whereas the 12 s to 20 s Rayleigh waves sample the middle-lower crust up to 25–30 km of depth. Love waves are characterized by a depth

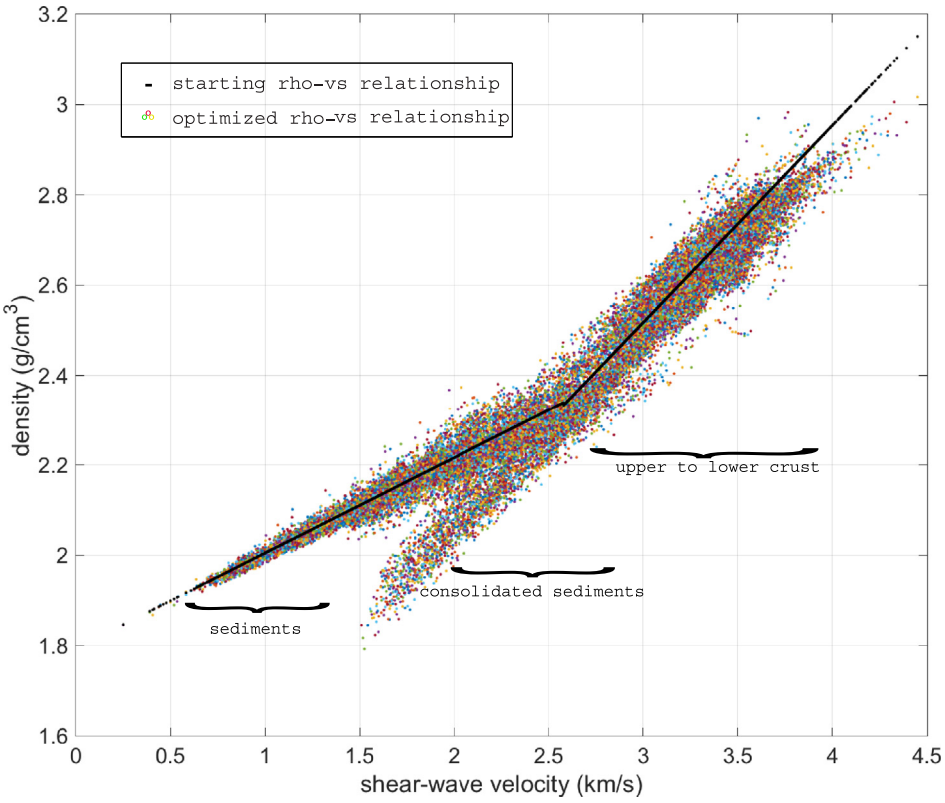

Fig. 7. Comparison between the SII-ρ-v_s relationships and the starting ρ-v_s scaling factors (black line).

resolution shallower than Rayleigh waves (see Fig. 3). Group velocity tomography maps at 4 s, 8 s, 12 s, and 20 s for Rayleigh and Love waves are shown in Fig. 8 a,b. Low group velocity is found at shorter periods evidencing a strong correlation between the Po plain soft sediments and low velocities. Note that the negative group velocity anomalies follow the foredeep sediments close to the Apennines as highlighted by the geophysical information from oil exploration and research undertaken since 1960 (e.g., Pieri and Groppi, 1981; Cassano et al., 1986; Ambrosetti et al., 1987). Positive anomalies (+20%) are found below the Alps and Apennines. Rayleigh and Love group velocity tomography maps agree with the Molinari et al. (2015) calculated group velocities for periods higher than 8 s (discrepancies are lower than 0.100 km/s in the investigated area). More significant differences up to 0.15 km/s, and 0.20 km/s in the Rayleigh and Love group velocities, respectively, are found at shorter periods and close to the Alpine and Apennine margins where the model complexity could affect the measure of the dispersion properties.

Shear-wave velocity models are obtained by inverting local dispersion properties retrieved from surface wave tomography. The shear-wave velocity profiles crossing the deep basin from S to N at longitudes from 10°E to 12.2°E are shown in Fig. S3. Along the profiles, the contouring of shear-wave velocities is performed with a 0.1-degree step in the velocity range from 0.5 km/s to 4.0 km/s. At shallow depth, low shear-wave velocities are found within the plains (Po and Venetian) and at depth for Pliocene–Quaternary sediments along the Northern Apennines. Fast shear-wave velocities at shallow depth are consistent with high P-wave anomalies related to the presence of Mesozoic limestone units.

Following the optimization of both shear velocities and densities, we also obtain an updated ρ-v_s correlation coefficient (α_m). We observe a normal distribution around the initial values with a standard deviation of about 10% of the starting value (Fig. 7). An anomalous greater difference is observed between 1.5 and 2.5 km/s, which, following Molinari et al. (2015), corresponds to Oligo-Miocene and Paleocene-Eocene units which were deposited during the thrusting of the southern Alpine front and the initial building of the Alpine belt, respectively.

Depth sections of the resulting SII-v_s and density models, up to 10 km depth, after the first SII iteration, are plotted in Figs. 9 and 10. The a posteriori standard deviation, associated with the density parameters, ranges between 32 and 66 kg/m^3. Higher reliability of the density model, associated with smaller values of standard deviation, is obtained within the upper-mid crust (depths < 12 km).

This is evidenced by the seismic misfit obtained for both the seismic and the SII-v_s model after the first (and last) iteration, with lower residuals between periods of 7 and 14 s (Fig. 11).

The most prominent feature of the SII models, is a high shear-wave velocity (≥3.3 km/s) density (≥2.2 kg/m^3) structure between the accretionary wedge of Northern Apennines and the foothills of the Southern Alps, at the northeastern margin of the Ferrara arc. This structure, which is buried below the thick Pliocene-Quaternary succession that fills-in the Po plain, characterizes our study area at depths ranging from 6 to 10 km (Figs. 9 and 10) and forms an extended arc-shaped 100 km long 40 km wide structure. Moderate to high local seismicity ($M_L \geq 4$) is concentrated at the edge of the transition from high to low compressibility, in the middle and southwest of the investigated area. The hypocenters of the 2012 earthquake sequence appear to outline an inherited major Mesozoic extensional fault (Carannante et al., 2015), which may bound domains with different litho-mechanical properties.

The gravity data field reproduced by the resulting SII density model is shown in Fig. 12 a). We obtain a mean gravity data misfit (9) (Fig. 12 b) of 4.10 mgals (with respect to 56.34 mgals of the seismological model scaled into a density model) and a data variance reduction (10) of 94.03% (with respect to 34.28% of the scaled seismological model).

Gravity residuals reveal that Bouguer gravity anomalies are very well fitted except in some random spots, mostly placed beneath the Apennines chain, and the unconsolidated Holocene deposits in the middle and north-east of the study area. Positive residuals are localized

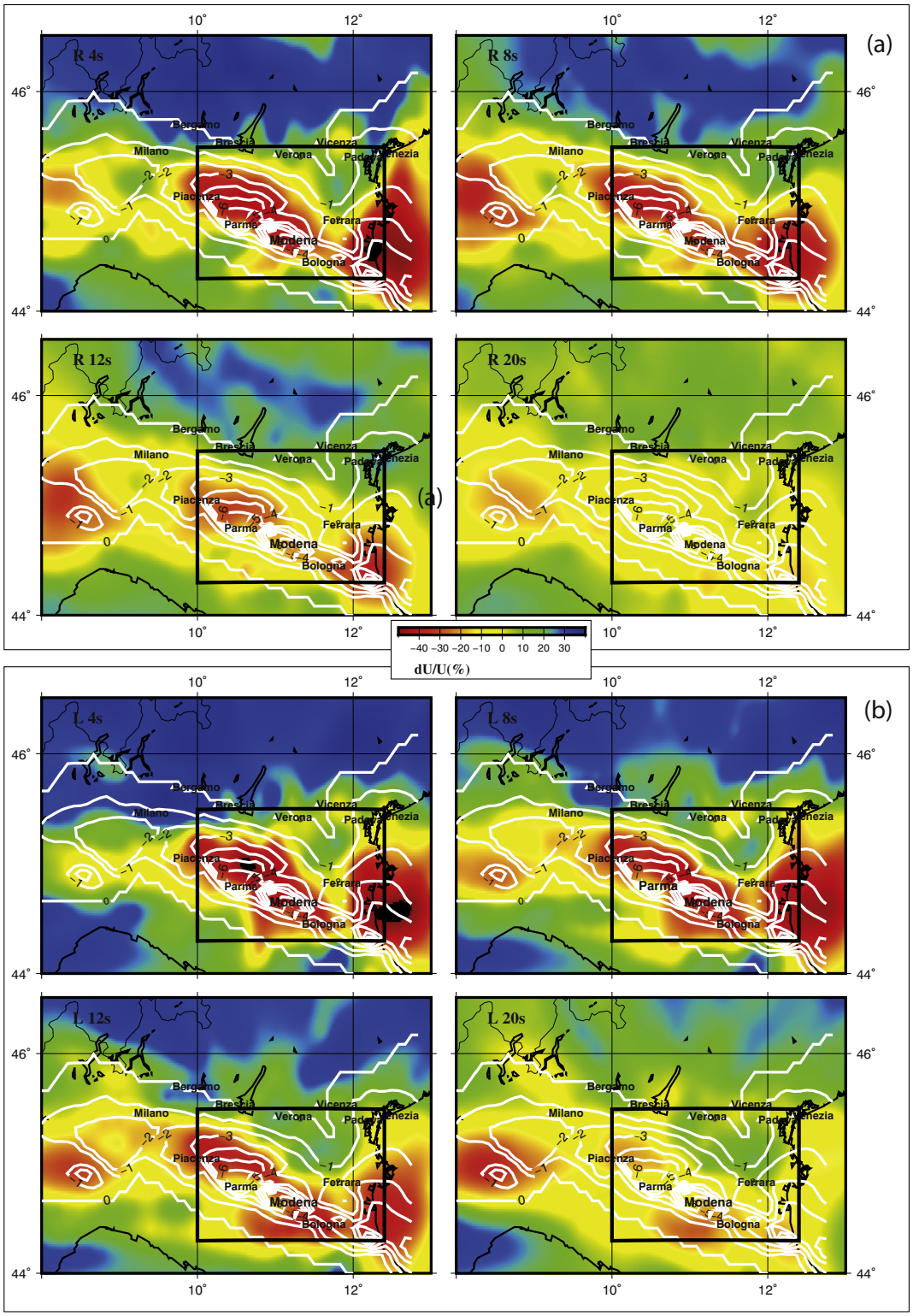

Fig. 8. (a) Rayleigh and (b) Love wave group velocity map through the Po plain at the periods indicated in the left upper corner of each panel. Blues indicate group velocities faster than average and reds slower than group velocity average. The black rectangle delimits the study area. Contours at 1 km intervals (white thick lines) define the thickness of sediments. (For interpretation of the references to color in this figure legend, the reader is referred to the web version of this article.)

where the SII model shows in-depth anomalous high velocity-density structures, thus justifying a possible additional bulk density.

5. The crustal model and the correlation with known geological and structural features

A comprehensive look at the recovered 3D shear-wave velocity and mass density evidence some important shared features which can be correlated to known geological structures.

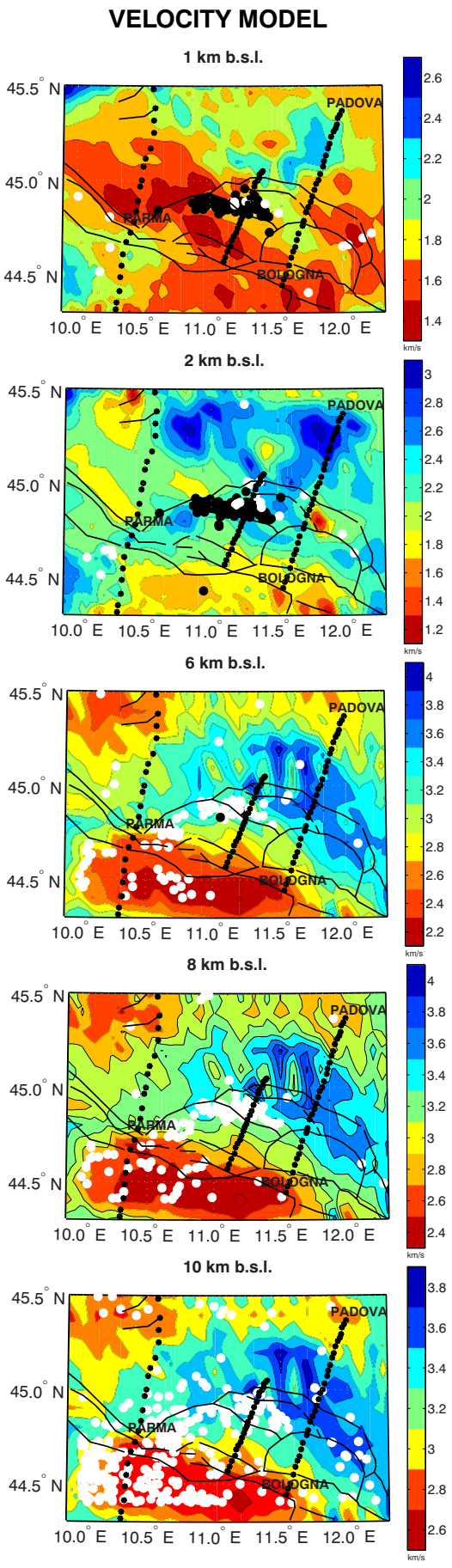

Fig. 9. Depth sections of the v_s perturbations in our optimized SII- v_s model. Seismic events from ISC catalogue with ML > 4, relocalized by Carannante et al. (2015) are superimposed (white and black dots). Black balls indicate the 2012 seismic events. The traces of cross sections A, B and C (black stars) and main tectonic lines (black lines) are also indicated.

The foredeep basin domain is well expressed by the group velocity anomaly maps (Fig. S3), particularly at short periods (4–8 s), as a low-velocity anomaly running along the Apennines plunging southward in the Ferrara region and eventually extending into the northern Adriatic Sea. The narrowing of the basin in the region of the Ferrara arc is well reproduced, as well as the southern "nose" of the foreland, characterized by higher values likely given by carbonate rocks at shallow depth.

Deeper, higher velocity-density structures replace the Pliocene-Quaternary successions and the 8 km depth maps (Figs. 9 and 10) show the clastic foredeep sediments tapering out south-eastward. The distribution of high values of SII shear velocity (3.6–4 km/s – Fig. 9) and densities (2.7–3 g/cm^3 – Fig. 10) follows the extent of the carbonate rocks: in the foreland, in the Ferrara folds and the thrust units close to the pede-Apennines.

The Ferrara arc is part of a group of three main structural arcs buried underneath the Po Plain, namely from west to east: the Monferrato arc, the Emilia arc, and the Ferrara-Romagna arc. The origin of this system of arcs seems related to the inherited Mesozoic paleogeography and the ensuing lithostratigraphic characteristics of the units affected by thrusting (Castellarin and Vai, 1986; Fantoni and Franciosi, 2010; Masetti et al., 2012). These three arcs represent at the broad scale the termination of the external northern Apenninic arc and the origin of their arcuate shape is still debated (Montone and Mariucci, 1999). It is hypothesized to be due to:

a) transversal NE-SW oriented lineaments that accompanied the emplacements of the arcs (Pieri and Groppi, 1981);
b) different shortening values, increasing from west to east (Pieri and Groppi, 1981; Gasperi et al., 1986; Royden et al., 1987)
c) the presence of rigid crustal blocks such as intrusive volcanic bodies or the elevation of crystalline basement which prevented lateral propagation of the tectonic detachment area (Castellarin and Vai, 1986)
d) the bending of a previous straight belt with vertical-axis rotation during thrust emplacement (Speranza et al., 1997).

Considering the high susceptibility toward diagenetic alterations of carbonates (Anselmetti and Eberli, 1993; Brigaud et al., 2010), our results suggest that the arc-shaped arrangement of the Po Plain front can be explained by admitting a more rigid behaviour of the zones with high positive anomaly linked to structural highs of the crystalline basement and to strengthening of their cover through magmatic events (Castellarin and Vai, 1986). Additionally, the localization of the 2012 seismic events evidences that active tectonic loading occurs at the margins of this rigid volume.

To examine in detail the recovered structures, three geological cross sections from the Apennines to the Southern Alps, derived from seismic studies, are matched with vertical sections cutting across the 3D distributions of the density and shear velocity (Figs. 13, 14 and 15). The three cross sections (see Fig. 1 for the localization) sample the investigated area from West (Fig. 13) to East (Fig. 15), crossing the area of the 2012 seismic sequence in Emilia (Fig. 14).

In our modelling, we are not imposing constraints about the interfaces or overhang structures shown in the geological sections. It is well known that instability in the inversion of geophysical data generally results in situations where small changes in data result in large fluctuations in a model. The degree of instability could be reduced either by imposing constraints or by including an extra independent data set to the inversion procedure. Because the information on the overhang

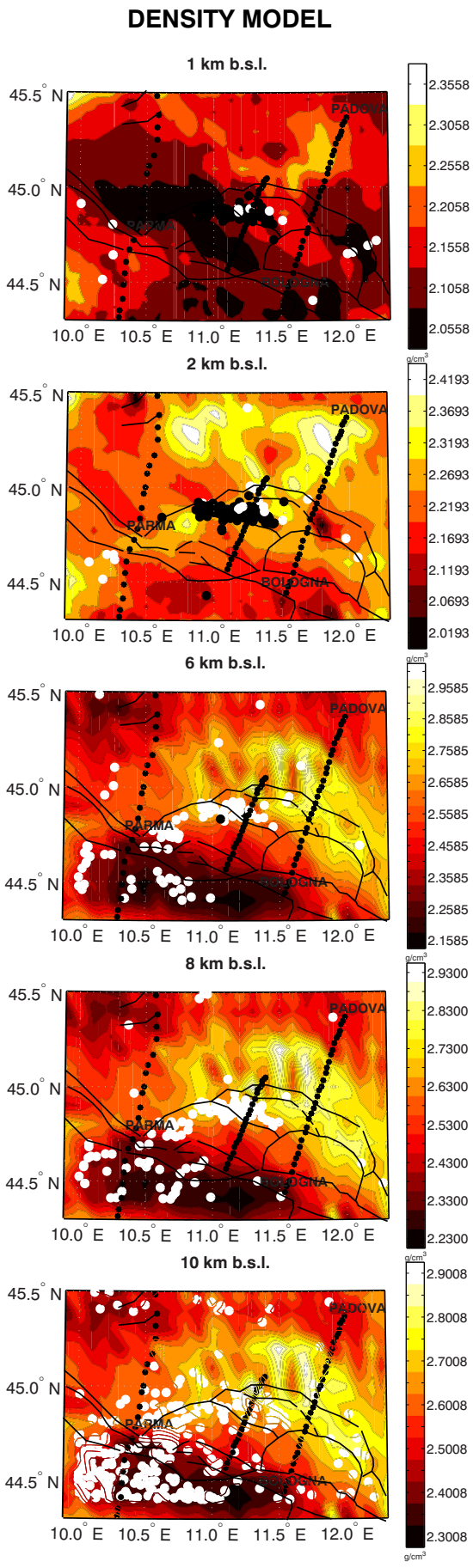

Fig. 10. Depth sections of the ρ perturbations in our optimized SII density model. Seismic events from ISC catalogue with ML > 4, relocalized by Carannante et al. (2015), are superimposed. Black balls indicate the 2012 seismic events (white and black dots). The traces of cross-sections A,B and C (black stars) and main tectonic lines (black lines) are also indicated.

structures comes from isolated boreholes that reach a maximum 5 km of depth, and from the interpretation of old seismic sections that cannot resolve at depth these structures, we preferred not to constrain their interfaces. Moreover, as remarked in the paper, the carbonatic rocks show a high degree of Vs variation that we preferred to explore without imposing possible lateral inhomogeneities. In our case, the inversion is stabilized by reducing the resolution of the inverted Vs model, and by combining surface wave with density data.

Although the main structures are well represented by all the models, a fine comparison between the geological models derived from seismic interpretation and our model evidences mismatches, especially below 6–8 km of depth, where the a posteriori standard deviation values associated to SII model are higher (7% compared to 2–3% of the density value in the shallower layers).

Section A in Fig. 13, is characterized by a thick and wide foredeep basin filled with Pliocene clastic sediments, with thrust faults mostly located close to the pede-Apennines. The foredeep basin is narrower and more segmented in the sectors crossed by sections B, and C, (Figs. 14, 15) and the thrust faults extend into the foreland, to originate the Ferrara folds (Fig. 14). The Mesozoic carbonates units are heavily involved in the deformation, all the way to the thrust front.

About our results, v_S and densities along the cross section A (Fig. 13) show the following points:

1) The wide foredeep basin filled with clastic sediments is well represented in the first kilometers, both in the velocity and the density values; low values of the parameters are found up to 5 km of depth.
2) The best image of the “pristine” foreland region is possibly given by the central segment of the density section, with values rapidly increasing with depth. The low values of density and shear velocity at depth, beneath the Apennines, may be related to the stacking of thrust sheets, largely composed of clastic rocks deposited in previous foredeep basins. Deep fluids migrating up-dip toward the foreland (e.g., Piana Agostinetti et al., 2011) can also contribute to decreasing the rock matrix.
3) To a large extent, foreland units below the clastic sediments are represented by Mesozoic carbonates. As discussed by Brigaud et al. (2010), sonic velocities in carbonates are controlled by the combined effect of depositional lithology and several post-depositional processes such as cementation or dissolution that lead to an extraordinarily wide range in velocities. Hence, fractures and faults can change the carbonate rock properties. Likewise, active tectonics in the area could explain the shear weakening/strengthening of the carbonate rocks.

The cross-section B (Fig. 13) intersects the 2012 Emilia seismic sequence.

Under the Apennines, the structural trends of the foredeep basin, filled with the Pliocene-Quaternary clastic sediments, are similar to those observed in section A, with low density and shear velocity values at depth. Conversely, latitudes > 44.75° are characterized by high density-velocity values which are part of a wider structure which extends beneath the external margin of the Ferrara arc toward the Alps and the Adriatic Sea. The seismic events of the 2012 Emilia sequence are located within this sector and the change of the elastic properties at a depth of about 5 km in the crustal structure is consistent with the crustal model locally inferred to invert for source moment tensors (e.g., Malagnini et al., 2012).

Fig. 15 shows the cross-section C located in the easternmost part of

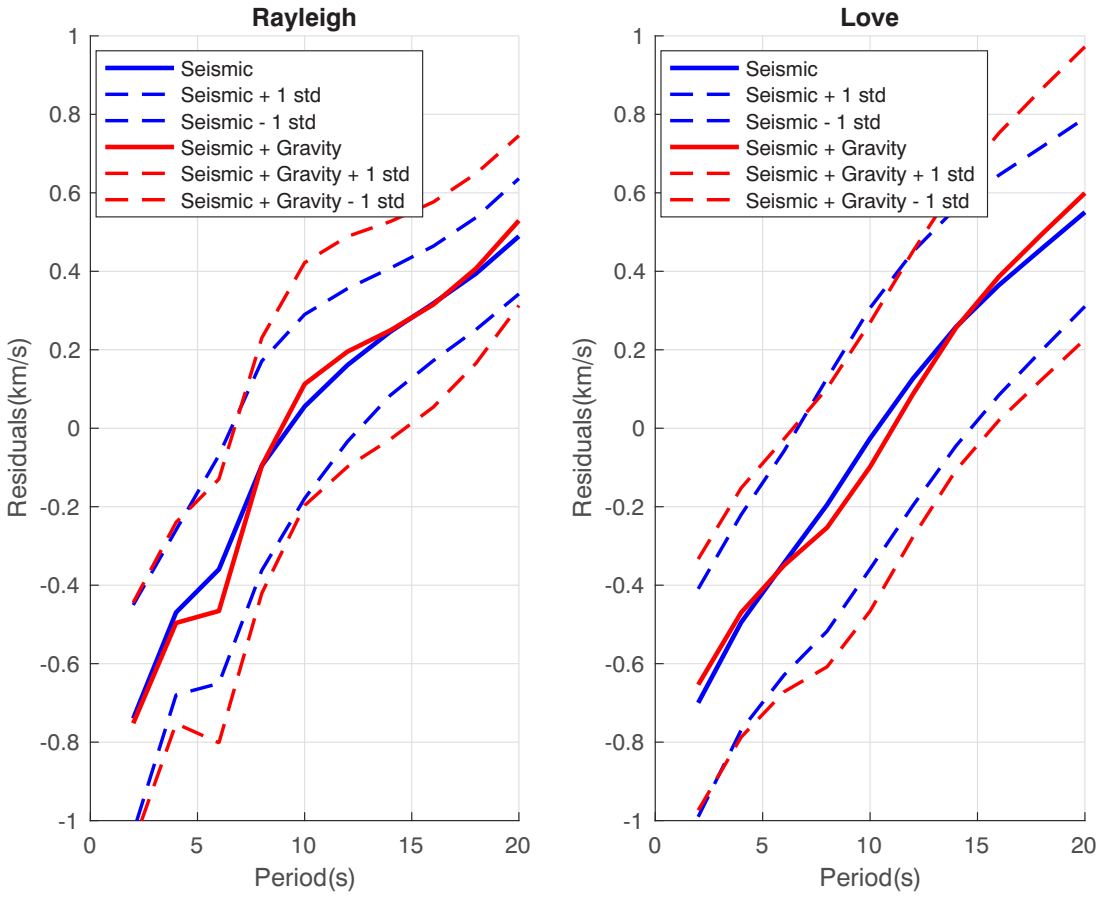

Fig. 11. Seismic data misfit for group velocity ad different periods in the seismic and SII velocity model for a) Rayleigh and b) Love waves.

the investigated area. The sampled crustal structure extends from the Apennines to the north, close to the border between the Po plain and the Venetian plain (where the sedimentary cover is considerably thinner). The observations made for cross-sections A and B can be extended to cross section C. The sediments close to the Apennines are thicker than in the northern part, and the pattern of density and velocity values (Fig. 15 b and c) is consistent with these depth variations. The aspect of the "pristine" foreland, in the central segment of section C, is similar to that observed in the central segment of section A. The Mesozoic carbonates are faulted at depths ranging from 2 to 10 km, especially beneath the Ferrara folds. A thinning of the clastic sedimentary cover going from the Apennines to the north is consistent with the mass density and the shear velocity sections (see Fig. 15 b and c). An almost flat layer between 3 km and 5 km depth, extending for about 50 km from the Ferrara folds, is characterized by density values between 2 and 2.1 g/cm^3 and v_S between 1.5 and 2 km/s. This shear weakening zone could be related to the presence of fluids.

In summary, the previous comparisons point out:

a) the lateral heterogeneities are often marked by tectonic discontinuities beneath the Northern Apennines and the structural high close to the 2012 seismic sequence.
b) undeformed Po Plain foredeep clastic units can be recognized by low velocities/densities.
c) the Mesozoic carbonates are not univocally defined in our inversions. This could be a limit of our methods or an effect due to their heterogeneity in physical properties.

Starting models are preliminarily obtained by surface wave tomography inversions at a larger grid than the subsequent gravity data inversion. This could have contributed to smoothed heterogeneities on a smaller scale. Moreover, the complex structural framework, the active tectonics, and thermal convection phenomena may cause variations in mineral composition, porosity, pore type, saturation, and pore pressure, making difficult the petrophysical characterization of carbonates.

6. Conclusions

The possibility to integrate high quality Love and Rayleigh group velocity measurements and a high resolution (1 km × 1 km) Bouguer gravity anomaly data-set enabled us to constrain the crustal structure of the Po plain, up to 20 km depth (with accuracy of the order of 0.033° × 0.033° within the first 12 km) and to derive new 3D shear-wave velocity (a posteriori seismic covariance of 0.250 km/s for depths from 0. to 4 km, 0.150 km/s from depths from 4 to 8 km and 0.80 km/s for depths from 8 to 20 km) and mass density models (a posteriori standard deviation which ranges between 32 and 66 kg/m^3) that are jointly checked for both seismic and gravity data (data variance reduction of 94.03%). The models:

1) enable us to obtain a seismological and gravity data consistent 3D phase relationship between the isotropic shear-wave velocity and the density structure, which is optimized within the a priori value limits [−14 + 8] %;
2) enable us to make novel inferences on the lateral heterogeneities which characterize the buried tectonic structures.

We are confident that the fully 3D map of the density-v_s scaling relationship, that is well suited for both the seismological and mineral physics communities, is a step forward for a better understanding of the tectonic features and geophysical processes that occur within this complex region, as well as a contribution for improving earthquake

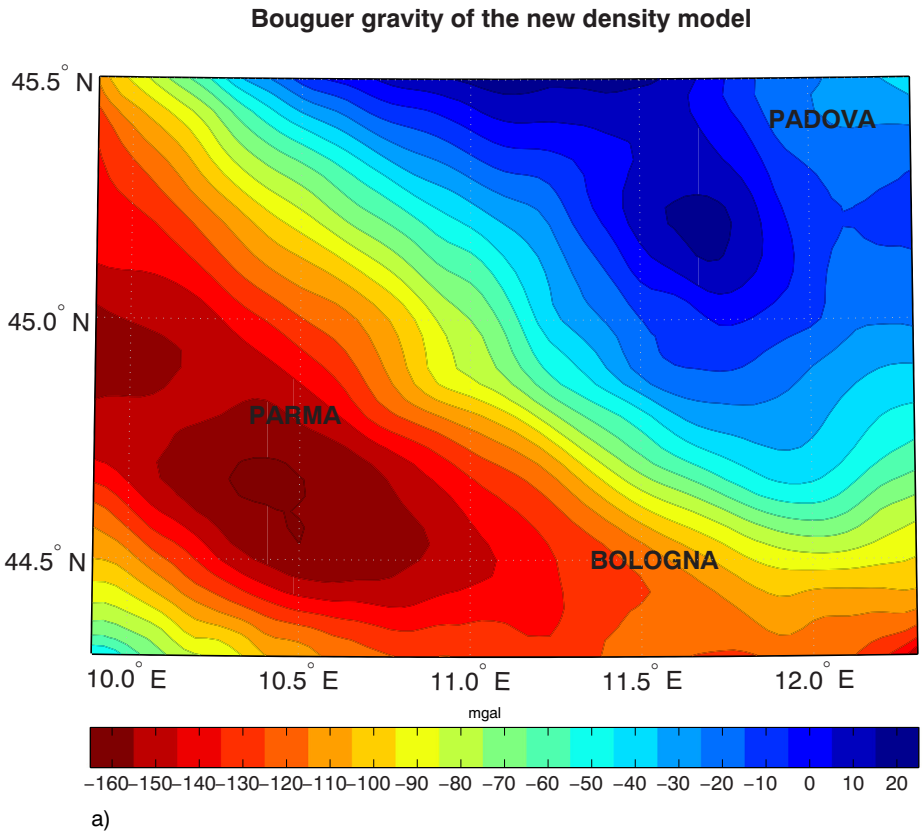

a)

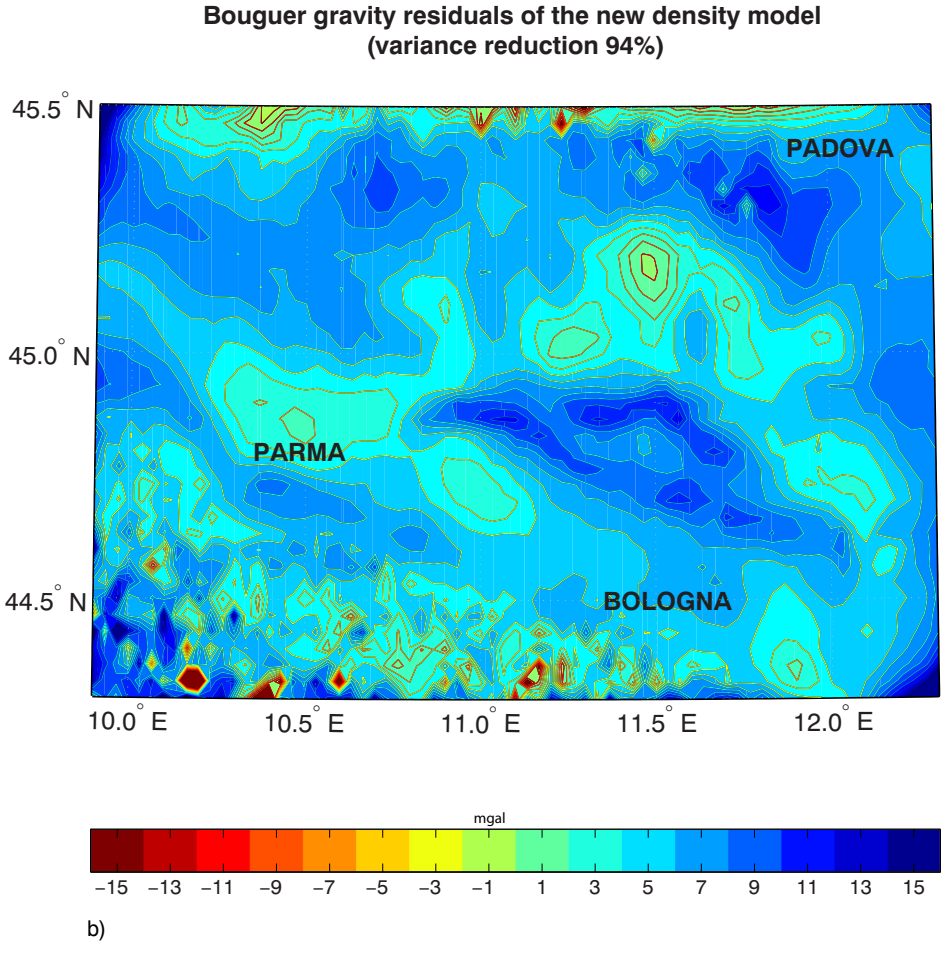

b)

(caption on next page)

Fig. 12. a) Bouguer anomaly map reproduced by SII-ρ model in Fig. 8. b) Gravity misfit with respect to observations in Fig. 4 is 4.10 mgals and variance reduction is 94.03%.

location or studies of seismic sources.

Additionally, as new knowledge with respect to previous literature, our results identify:

a) at shallow depths a narrow volume of shear velocities ranging from 1.5 to 2.7 km/s and of densities in the interval [1.8 to 2.3] g/cm^3 which possibly belongs to the consolidated clastic sediments of the Po Plain foredeep basin;
b) at depths ranging from 6 to 10 km the presence of a high shear-wave velocity (≥3.3 km/s) -density (≥2.2 kg/m^3) body which is buried below the thick Pliocene-Quaternary succession that fills-in the Po plain and forms an extended arc-shaped 100 km long and 40 km wide structure. The finding is in agreement with a recent tomographic study by Kästle et al. (2018). The 2012 Emilia seismic sequence characterized by six earthquakes with M > 5 took place at the southern margin of this body, along a 50 km E-W trending segment. It is therefore not excluded that active tectonic stress can be focussed at the edges of this rigid structure.

Supplementary data to this article can be found online at https://doi.org/10.1016/j.tecto.2018.10.018.

Acknowledgments

The interpretation given in this report stems from the activities carried out by the authors from 2012 to 2015 within the DPC-INGV S1 Project (base-knowledge improvement for assessing the seismogenic potential of Italy). Seismological data are available from National Seismic Network (RSN https://doi.org/10.13127/SD/X0FXnH7QfY), operated by the Istituto Nazionale di Geofisica e Vulcanologia (INGV),

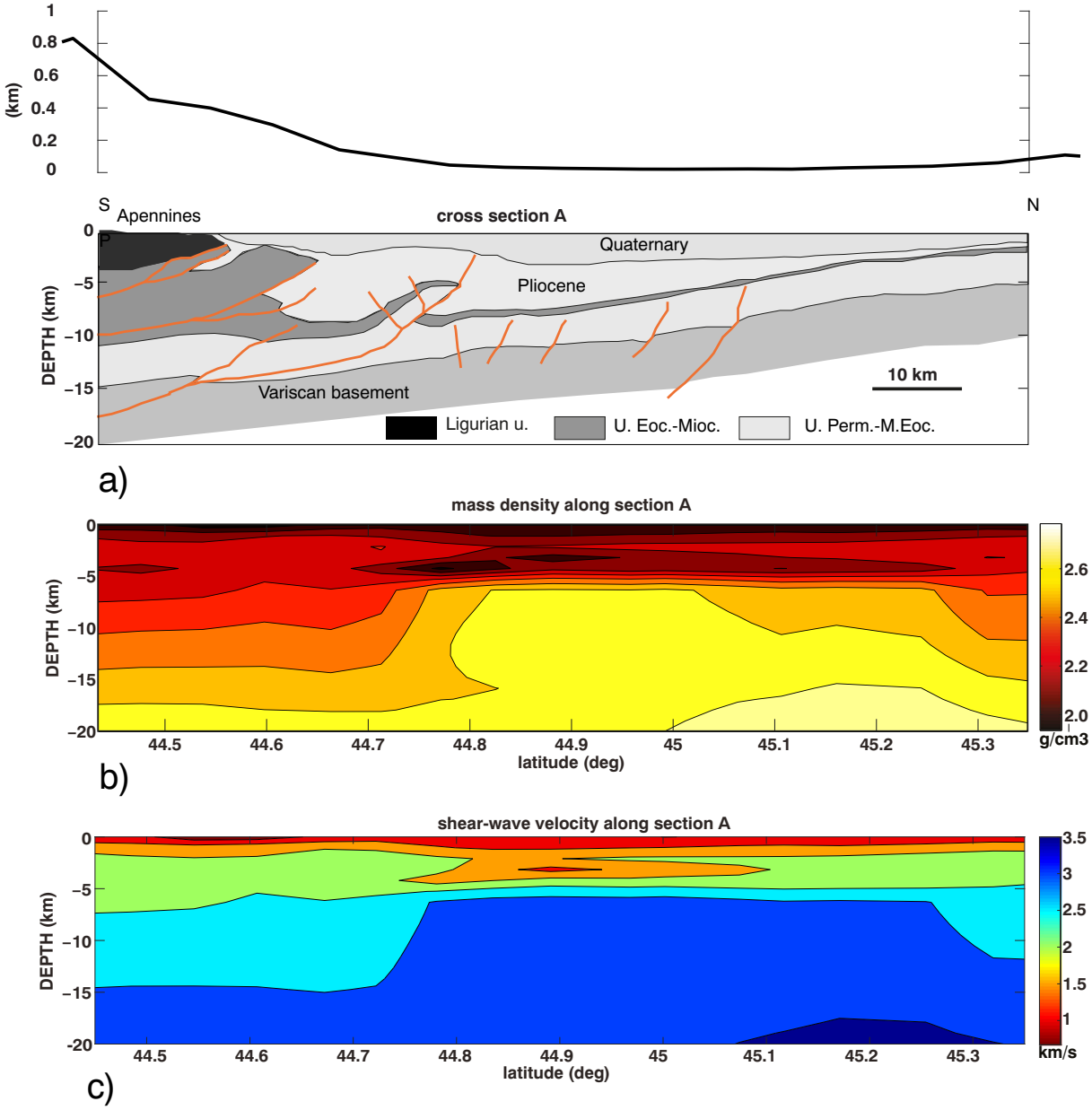

Fig. 13. Profile A (after Fantoni and Franciosi, 2010) as shown in Fig. 1. (a) simplified geological structure, (b) density model, (c) shear-wave velocity model.

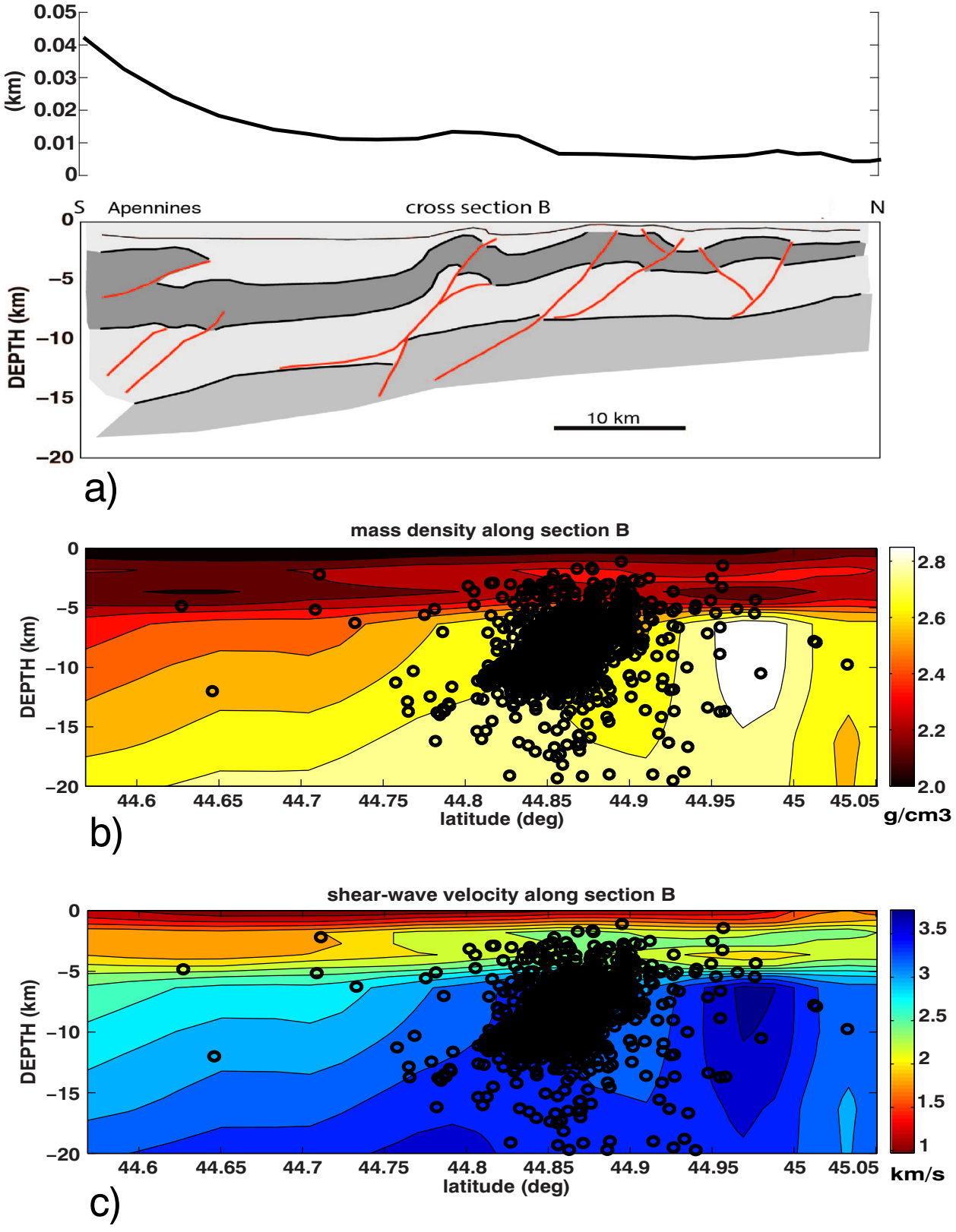

Fig. 14. Profile B, as shown in Fig. 1. (a) simplified geological structure (modified after Bonini et al., 2014); stratigraphic units as in Fig. 12, (b) density model, (c) shear-wave velocity model. Seismic sources (black circles) from the ISC catalogue, with $M_l \geq 2.5$, relocalized by Carannante et al. (2015) are superimposed on (b) and (c) and evidence the 2012 Emilia earthquakes sequence crossed by the profile.

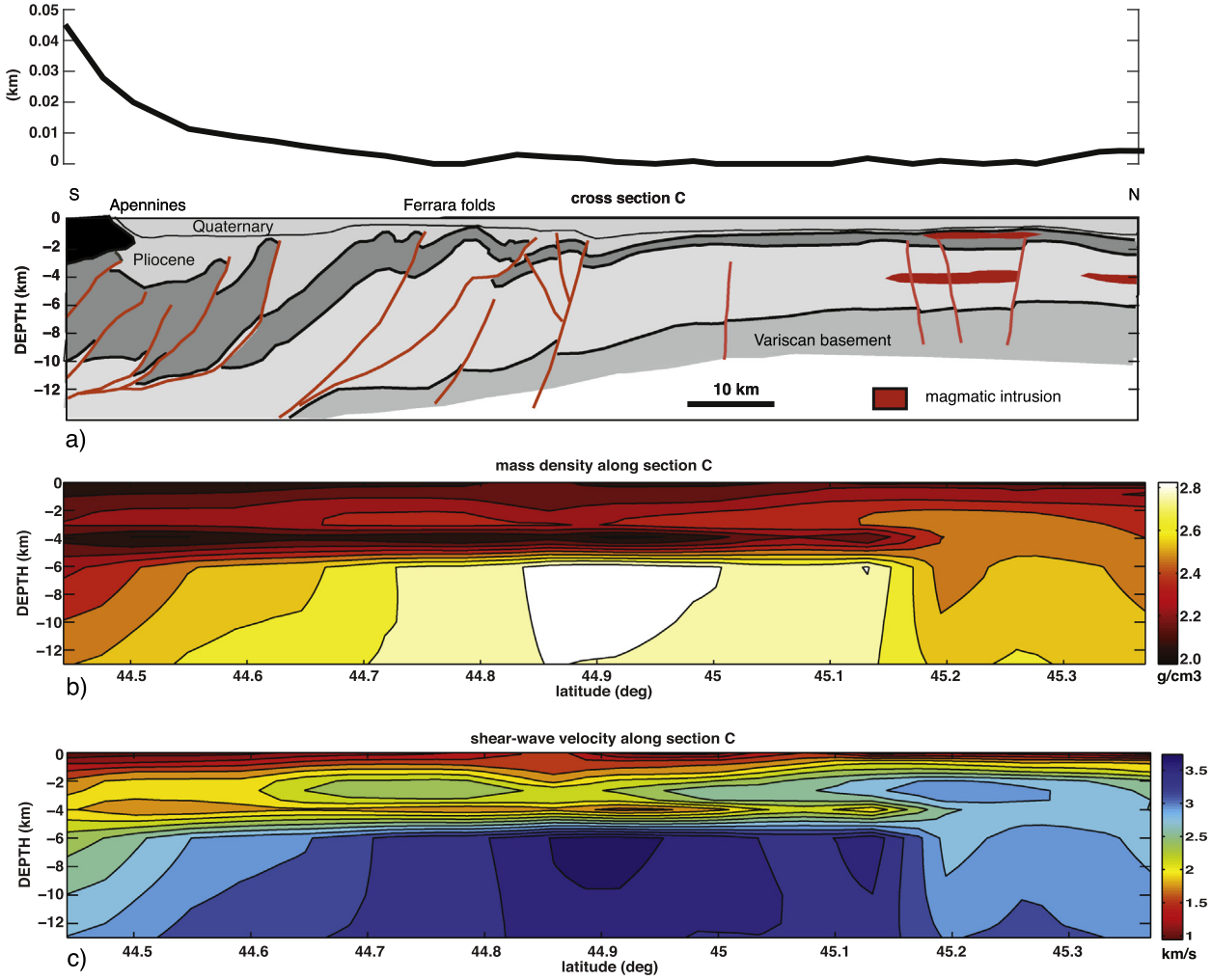

Fig. 15. Profile C (modified after Picotti and Pazzaglia, 2008 and Cassano et al., 1986), as shown in Fig. 1. (a) simplified geological structure,; stratigraphic units as in Fig. 10, (b) density model, (c) shear-wave velocity model.

and from a regional network (OX https://doi.org/10.7914/SN/OX) operated by the Istituto Nazionale di Oceanografia e di Geofisica Sperimentale (OGS). Accelerometric data are available at the **ISMD (INGV Strong Motion Data web portal: http://ismd.mi.ingv.it/)** providing in quasi-real time the strong motion waveforms related to the Italian earthquakes with local magnitude (M_L) ≥ 3.0, and from RAN (Rete Accelerometrica Nazionale) http://ran.protezionecivile.it/IT/index.php.

We thank Tatiana Yanovskaja and Nick Rawlinson for allowing the use of surface wave tomography codes.

References

Ambrosetti, P., Bartolini, C., Bosi, C., Carraro, F., Ciaranfi, N., Panizza, M., Papani, G., Vezzani, L., Zanferrari, A., 1987. Neotectonic map of Italy (scale 1:500,000). Quad. Ric. Sci. 4, 114.

Anselmetti, F.S., Eberli, G.P., 1993. Controls on sonic velocity in carbonates. PAGEOPH 141 (2/3/4), 287–323.

Argnani, A., Barbacini, G., Bernini, M., Camurri, F., Ghielmi, M., Papani, G., Rizzini, F., Rogledi, S., Torelli, L., 2003. Gravity tectonics driven by Quaternary uplift in the Northern Apennines: insights from the La Spezia-Reggio Emilia Geo-Transect. Quat. Int. 101 (102), 13–26.

Barnaba, C., Laurenzano, G., Moratto, L., Sugan, M., Vuan, A., Priolo, E., Romanelli, M., Di Bartolomeo, P., 2014. Strong-motion observations from the OGS temporary seismic network during the 2012 Emilia sequence in northern Italy. Bull. Earthq. Eng. 12, 2165–2178. https://doi.org/10.1007/s10518-0149629-6.

Barzaghi, R., Borghi, A., Carrion, D., Sona, G., 2007. Refining the estimate of the italian quasi-geoid. Boll. Geodesia Sci. Affinity 3, 145–160.

Basili, R., Valensise, G., Vannoli, P., Burrato, P., Fracassi, U., Mariano, S., Tiberti, M., Boschi, E., 2008. The Database of Individual Seismogenic Sources (DISS), version 3: summarizing 20 years of research on Italy's earthquake geology. Tectonophysics 453, 20–24. https://doi.org/10.1016/j.tecto.2007.04.014.

Beaty, K.S., Schmitt, D.R., Sacchi, M., 2002. Simulated annealing inversion of multimode Rayleigh wave dispersion curves for geological structure. Geophys. J. Int. 151, 622–631. https://doi.org/10.1046/j.1365-246X.2002.01809.x.

Benedetti, L.C., Tapponnier, P., Gaudemer, Y., Manighetti, I., Van der Woerd, J., 2003. Geomorphic evidence for an emergent active thrust along the edge of the Po plain: the Broni–Stradella fault. J. Geophys. Res. 108 (B5), 2238. https://doi.org/10.1029/2001JB001546.

Bonini, L., Toscani, G., Seno, S., 2014. Three-dimensional segmentation and different rupture behavior during the 2012 Emilia seismic sequence (Northern Italy). Tectonophysics 630, 33–42.

Borghi, A., Carrion, D., Sona, G., 2007. Validation and fusion of different databases in preparation of high-resolution geoid determination. Geophys. J. Int. 171 (2), 539–549. https://doi.org/10.1111/j.1365-246X.2007.03541.x.

Brigaud, B., Vincent, B., Durlet, C., Deconinck, J.F., Blank, P., Trouiller, A., 2010. Acoustic properties of ancient shallow-marine carbonates: effects of depositional environments and diagenetic processes (Middle Jurassic, Paris Basin, France). Int. J. Sediment Res. 80, 791–807. https://doi.org/10.2110/jsr.2010.071.

Brocher, T.M., 2008. Compressional and shear-wave velocity versus depth relations for common rock types in Northern California. Bull. Seismol. Soc. Am. 98, 950–968. https://doi.org/10.1785/0120060403.

Burrato, P., Ciucci, F., Valensise, G., 2003. An inventory of river anomalies in the Po plain, Northern Italy: evidence for active blind thrust faulting. Ann. Geophys. 46 (5), 865–882.

Carannante, S., Argnani, A., Massa, M., D'Alema, E., Lovati, S., Moretti, M., Cattaneo, M., Augliera, P., 2015. The May 20 (MW 6.1) and 29 (MW 6.0), 2012, Emilia (Po Plain, northern Italy) earthquakes: new seismotectonic implications from subsurface geology and high-quality hypocenter location. Tectonophysics 655, 107–123. https://doi.org/10.1016/j.tecto.2015.05.015.

Caratori Tontini, F., Graziano, F., Cocchi, L., Carmisciano, C., Stefanelli, P., 2007. Determining the optimal Bouguer density for a gravity data set: Implications for the

isostatic setting of the Mediterranean Sea. Geophys. J. Int. 169, 380–388.
Cassano, E., Anelli, L., Fichera, R., Cappelli, V., 1986. Pianura Padana — interpretazione integrata di dati geofisici e geologici. In: 73 Congr. Soc. Geol. Italiana, 29 September–4 October 1986, Roma.
Castellarin, A., Vai, G.B., 1986. South alpine versus Po Plain Apenninic arcs. In: Wezel, F.C. (Ed.), The Origin of Arcs. Elsevier Science Publishers B. V., Amsterdam, pp. 253–280.
Castellarin, A., Eva, C., Giglia, G., Vai, G.B., 1985. Analisi strutturale del fronte appenninico padano. Giorn. Geol. 47, 47–76.
Chiarabba, C., Jovane, L., DiStefano, R., 2005. A new view of Italian seismicity using 20 years of instrumental recordings. Tectonophysics 395, 251–268. https://doi.org/10.1016/j.tecto.2004.09.013.
Ditmar, P.G., Yanovskaya, T.B., 1987. Generalization of the Backus-Gilbert method for Estimation of the Horizontal Variations of surface wave velocities, Izvestiya. Earth Physics 23 (6), 470–477.
Fantoni, R., Franciosi, R., 2010. Tectono-sedimentary setting of the Po Plain and Adriatic foreland. Rend. Fis. Accad. Lincei 21 (1), 197–209. https://doi.org/10.1007/s12210-010-0102-4.
Forsberg, R., Tscherning, C.C., 2008. GRAVSOFT, Geodetic Gravity Field Modelling Programs (Overview Manual).
Gabriels, P., Snieder, R., Nolet, G., 1987. In situ measurements of shear wave velocity in sediments with higher-mode Rayleigh waves. Geophys. Prospect. 35, 187–196. https://doi.org/10.1111/j.1365-2478.1987.tb00812.x.
Gasperi, G., Gelati, R., Papani, G., 1986. Neogene evolution of the Northern Apennines on the Po Valley side. J. Geol. 48 (1/2), 187–195.
Ghielmi, M., Minervini, M., Nini, C., Rogledi, S., Rossi, M., 2013. Late Miocene–Middle Pleistocene sequences in the Po Plain—Northern Adriatic Sea (Italy): the stratigraphic record of modification phases affecting a complex foreland basin. Mar. Pet. Geol. 42, 50–81. https://doi.org/10.1016/j.marpetgeo.2012.11.007.
Heiskanen, W.A., Moritz, H., 1990. Physical Geodesy. Institute of Physical Geodesy Technical University, Graz, Austria.
Herrmann, R.B., 2013. Computer programs in seismology: an evolving tool for instruction and research. Seismol. Res. Lett. 84, 1081–1088. https://doi.org/10.1785/0220110096.
ISIDE WORKING GROUP, 2010. Italian seismological instrumental and parametric database. http://iside.rm.ingv.it.
Kästle, E.D., El-Sharkawy, A., Boschi, L., Meier, T., Rosenberg, C., Bellahsen, N., Cristiano, L., Weidle, C., 2018. Surface wave tomography of the Alps using ambient-noise and earthquake phase velocity measurements. J. Geophys. Res. Solid Earth 123. https://doi.org/10.1002/2017JB014698.
Malagnini, L., Herrmann, R.B., Munafò, I., Buttinelli, M., Anselmi, M., Akinci, A., Boschi, E., 2012. The 2012 Ferrara seismic sequence: regional crustal structure, earthquake sources, and seismic hazard. Geophys. Res. Lett. 39, L19302. https://doi.org/10.1029/2012GL053214.
Masetti, D., Fantoni, R., Romano, R., Sartorio, D., Trevisani, E., 2012. Tectonostratigraphic evolution of the Jurassic extensional basins of the eastern southern Alps and Adriatic foreland based on an integrated study of surface and subsurface data. Am. Assoc. Pet. Geol. Bull. 96, 2065–2089. https://doi.org/10.1306/03091211087.
Meletti, C., D'Amico, V., Ameri, G., Rovida, A., Stucchi, M., 2012. Seismic hazard in the Po plain and the 2012 Emilia earthquakes. Ann. Geophys. 55, 623–629. https://doi.org/10.4401/ag-6158.
Molinari, I., Morelli, A., 2011. EPcrust: a reference crustal model for the european plate. Geophys. J. Int. 185 (1), 352–364. https://doi.org/10.1111/j.1365-246X.2011.04940.x.
Molinari, I., Argnani, A., Morelli, A., Basini, P., 2015. Development and Testing of a 3D seismic velocity model of the Po plain sedimentary basin, Italy. Bull. Seismol. Soc. Am. 105, 753–764. https://doi.org/10.1785/0120140204.
Montone, P., Mariucci, M.T., 1999. Active stress along NE external margin of the Apennines: the Ferrara arc, northern Italy. Geodynamics 28, 251–265.
Montone, P., Mariucci, M.T., 2015. P-wave Velocity, Density, and Vertical Stress Magnitude Along the Crustal Po Plain (Northern Italy) from Sonic Log Drilling Data. Pure Appl. Geophys. 172, 1547–1561.
Montone, P., Mariucci, M.T., Pierdominici, S., 2012. The Italian present-day stress map. Geophys. J. Int. 189, 705–716. https://doi.org/10.1111/j.1365-246X.2012.05391.x.
Nafe, J.E., Drake, C.L., 1957. Variation with depth in shallow and deep water marine sediments of porosity, density and the velocities of compressional and shear waves. Geophysics 22, 523–552. https://doi.org/10.1190/1.1438386.
Nolet, G., 1981. Linearized inversion of (teleseismic) data. In: Cassinis, R. (Ed.), The Solution of the Inverse Problem in Geophysical Interpretation. Plenum Press, New York, pp. 9–37. https://doi.org/10.1007/978-1-4684-3962-5_2.
Parker, R.L., 1994. Geophysical Inverse Theory. Princeton Univ. Press, Princeton, N. J9780691036342.
Piana Agostinetti, N., Bianchi, I., Amato, A., Chiarabba, C., 2011. Fluid migration in continental subduction: the Northern Apennines case study. Earth Planet. Sci. Lett. 302, 267–278. https://doi.org/10.1007/978-1-4684-3962-5_210.1016/j.epsl.2010.10.039.
Picotti, V., Pazzaglia, F.J., 2008. A new active tectonic model for the construction of the Northern Apennines mountain front near Bologna (Italy). J. Geophys. Res. 113 (B8), 1–24.
Pieri, M., Groppi, G., 1981. Subsurface Geological Structure of the Po Plain, Italy. CNR-PF Geodinamica, Agip, Milano, pp. 414. https://doi.org/10.13140/RG.2.1.4945.3840.
Pohànka, V., 1988. Optimum expression for computation of the gravity field of a homogeneous polyhedral body, Geophys. PRO 36, 733–751. https://doi.org/10.1111/j.1365-2478.1988.tb02190.x.
Pondrelli, S., Salimbeni, S., Ekstrom, G., Morelli, A., Gasperini, P., Vannucci, G., 2006. The Italian CMT dataset from 1977 to the present. Phys. Earth Planet. Inter. 159 (3–4), 286–303. https://doi.org/10.1016/j.pepi.2006.07.008.
Pondrelli, S., Salimbeni, S., Perfetti, P., Danecek, P., 2012. Quick regional centroid moment tensor solutions for the Emilia 2012 (northern Italy) seismic sequence. Ann. Geophys. 55, 615–621. https://doi.org/10.4401/ag-6146.
Rawlinson, N., Sambridge, M., 2003. Seismic traveltime tomography of the crust and lithosphere. Adv. Geophys. 46, 81–198. https://doi.org/10.1016/S0065-2687(03)46002-0.
Ritzwoller, M.H., Levshin, A.L., Ratnikova, L.I., Egorkin, A.A., 1998. Intermediate period group velocity maps across Central Asia, Western China, and parts of the Middle East. Geophys. J. Int. 134, 315–328.
Rovida, A., Camassi, R., Gasperini, P., Stucchi, M., 2011. CPTI11, the 2011 version of the Parametric Catalogue of Italian Earthquakes, Milano, Bologna. http://emidius.mi.ingv.it/CPTI/ (doi:10.6092/INGV.IT-CPTI11).
Royden, L., Patacca, E., Scandone, P., 1987. Segmentation and configuration of subducted lithosphere in Italy: an important control on thrust-belt and foredeep-basin evolution. Geology 15, 714–717.
Scognamiglio, L., Margheriti, L., Mele, F.M., Tinti, E., Bono, A., De Gori, P., Lauciani, V., Lucente, F.P., Mandiello, A.G., Marcocci, C., Mazza, S., Pintore, S., Quintiliani, M., 2012. The 2012 Pianura Padana emiliana seimic sequence: locations, moment tensors and magnitudes. Ann. Geophys. 55, 549–559. https://doi.org/10.4401/ag-6159.
Serpelloni, E., Faccenna, C., Spada, G., Dong, D., Williams, S.D., 2013. Vertical GPS ground motion rates in the Euro-Mediterranean region: new evidence of velocity gradients at different spatial scales along the Nubia–Eurasia plate boundary. J. Geophys. Res. 118, 6003–6024. https://doi.org/10.1002/2013JB010102.
Serpelloni, E., Vannucci, G., Anderlini, L., Bennett, R.A., 2016. Kinematics, seismotectonics and seismic potential of the eastern sector of the European Alps from GPS and seismic deformation data. Tectonophysics 688, 157–181. https://doi.org/10.1016/j.tecto.2016.09.026.
Sethian, J.A., Popovici, A.M., 1999. 3-D traveltime computation using the fast marching method. Geophysics 64, 516–523.
Speranza, F., Sagnotti, L., Mattei, M., 1997. Tectonics of the Umbria-Marche-Romagna Arc (central-northern Apennines, Italy): new paleomagnetic constraints. J. Geophys. Res. 102, 3153–3166.
Sugan, M., Vuan, A., 2014. On the ability of Moho reflections to affect the ground motion in northeastern Italy: a case study of the 2012 Emilia seismic sequence. Bull. Earthq. Eng. 12, 2179–2194. https://doi.org/10.1007/s10518-013-9564-y.
Tondi, R., de Franco, R., 2006. Accurate assessment of 3D crustal velocity and density parameters: Application to Vesuvius data sets. Phys. Earth Planet. Inter. 159, 183–201. https://doi.org/10.1016/j.pepi.2006.07.001.
Tondi, R., Cavazzoni, C., Morelli, A., 2012. Parallel “large” dense matrix problems: application to 3D joint inversion of seismological and gravity data. Comput. Geosci. 48, 143–156. https://doi.org/10.1016/j.cageo.2012.05.026.
Turrini, C., Angeloni, P., Lacombe, O., Ponton, M., Roure, F., 2015. Three-dimensional seismo-tectonics in the Po Valley basin, Northern Italy. Tectonophysics 661, 156–179. https://doi.org/10.1016/j.tecto.2015.08.033.
Vincenty, T., 1975. Direct and inverse solutions of geodesics on the ellipsoid with application of nested equations. Surv. Rev. 176, 88–93. https://doi.org/10.1179/sre.1975.23.176.88. XXIII.
Vuan, A., Russi, M., Panza, G.F., 2000. Group velocity tomography in the subantarctic Scotia Sea region. Pure Appl. Geophys. 157, 1337–1357.
Vuan, A., Klin, P., Laurenzano, G., et al., 2011. Far-source long-period displacement response spectra in the Po and Venetian Plains (Italy) from 3D wavefiled simulations. Bull. Seismol. Soc. Am. 101 (3), 1055–1072. https://doi.org/10.1785/0120090371.
Vuan, A., Sugan, M., Plasenci Linares, M.P., 2014. A reappraisal of surface wave group velocity tomography in the subantarctic Scotia Sea and surrounding ridges. Global Planet. Change 123, 223–238. https://doi.org/10.1016/j.gloplacha.2014.07.020.
Wathelet, M., Jongsman, D., Ornberger, M., 2004. Surface-wave inversion using a direct search algorithm and its application to ambient vibration measurements. Near Surf. Geophys. 2, 211–221. https://doi.org/10.3997/1873-0604.2004018.
Wiggins, R.A., 1972. The general linear inverse problem: implication of surface waves and free oscillations for Earth structure. Rev. Geophys. Space Phys. 110, 251–285. https://doi.org/10.1029/RG010i001p00251.
Xia, J., Miller, R.D., Park, C.B., 1999. Estimation of near-surface shear wave velocity by inversion of Rayleigh waves. Geophysics 64, 691–700. https://doi.org/10.1190/1.1444578.
Yamanaka, H., 2005. Comparison of the performance of heuristic search methods for phase velocity inversion in the shallow surface wave method. J. Environ. Eng. Geophys. 10, 163–173. https://doi.org/10.2113/JEEG10.2.163.
Yanovskaya, T.B., 1997. Resolution estimation in the problems of seismic ray tomography. Izv. Phys. Solid Earth 33 9 76 2765.
Yanovskaya, T.B., Ditmar, P.G., 1990. Smoothness criteria in surface wave tomography. Geophys. J. Int. 102, 63–72.
Yanovskaya, T.B., Kizima, E.S., Antonova, L.M., 1998. Structure of the crust in the Black Sea and adjoining regions from surface wave data. J. Seismol. 2, 303–316. https://doi.org/10.1023/A:1009716017960.
Yanovskaya, T.B., Antonova, L.M., Kozhevnikov, V.M., 2000. Lateral variations of the upper mantle structure in Eurasia from group velocities of surface waves. Phys. Earth Planet. Inter. 122 (1–2), 19–32. https://doi.org/10.1016/S0031-9201(00)00184-9.